

Key Points:

- E3SM is able to reproduce many features of the observed albedo-OLR histogram representing anvil cloud decay
- Three dimensional air parcel trajectories reveal anvil cloud lifetime of 15 h in both present and future warmer climate
- Thick anvil clouds contain more ice and have a larger optical depth in a warmer climate, while thin anvil clouds do not change substantially

Supporting Information:

- Supporting Information S1
- Movie S1

Correspondence to:

B. Gasparini,
blazg@uw.edu

Citation:

Gasparini, B., Rasch, P. J., Hartmann, D. L., Wall, C. J., & Dütsch, M. (2021). A Lagrangian perspective on tropical anvil cloud lifecycle in present and future climate. *Journal of Geophysical Research: Atmospheres*, 126, e2020JD033487. <https://doi.org/10.1029/2020JD033487>

Received 9 JUL 2020

Accepted 5 JAN 2021

A Lagrangian Perspective on Tropical Anvil Cloud Lifecycle in Present and Future Climate

Blaž Gasparini¹ , Philip J. Rasch² , Dennis L. Hartmann¹ , Casey J. Wall³ , and Marina Dütsch^{1,4} 

¹Department of Atmospheric Sciences, University of Washington, Seattle, WA, USA, ²Atmospheric Sciences and Global Change Division, Pacific Northwest National Laboratory, Richland, WA, USA, ³Scripps Institution of Oceanography, University of California San Diego, San Diego, CA, USA, ⁴Now at University of Vienna, Vienna, Austria

Abstract The evolution of tropical anvil clouds from their origin in deep convective cores to their slow decay determines the climatic effects of clouds in tropical convective regions. Despite the relevance of anvil clouds for climate and responses of clouds to global warming, processes dominating their evolution are not well understood. Currently available observational data reveal instantaneous snapshots of anvil cloud properties, but cannot provide a process-based perspective on anvil evolution. We therefore conduct simulations with the high resolution version of the exascale earth system model in which we track mesoscale convective systems over the tropical Western Pacific and compute trajectories that follow air parcels detrained from peaks of convective activity. With this approach we gain new insight into the anvil cloud evolution both in present day and future climate.

Comparison with geostationary satellite data shows that the model is able to simulate maritime mesoscale convective systems reasonably well. Trajectory results indicate that anvil cloud lifetime is about 15 h with no significant change in a warmer climate. The anvil ice mixing ratio is larger in a warmer climate due to a larger source of ice by detrainment and larger depositional growth leading to a more negative net cloud radiative effect along detrained trajectories. However, the increases in sources are counteracted by increases in sinks of ice, particularly snow formation and sedimentation. Furthermore, we find that the mean anvil cloud feedback along trajectories is positive and consistent with results from more traditional cloud feedback calculation methods.

Plain Language Summary Clouds can have both cooling and warming effects on climate. Storm clouds in the tropics preferentially cool the climate as they reflect a large fraction of sunlight back to space. Remains of storm clouds, also known as anvil clouds due to their typical shape, reside at very high altitudes and can persist for many hours after the initial intense rain events and extend over vast regions. They keep part of the terrestrial radiation within the atmosphere and therefore warm the climate, similarly to greenhouse gases. The transition from a very reflective storm cloud to a thin anvil cloud is not yet well understood despite playing an important role for tropical climate. We study such transitions with the help of climate model simulations in which we follow anvil clouds from their origin in storm clouds as they develop into thin anvil clouds and eventually disappear. The climate model allows us to study this process both in present-day as well as a warmer future climate. We find that in a warmer climate the storm clouds contain more ice and reflect more sunlight, which leads to more cooling, while the thin anvil clouds do not change much with warming.

1. Introduction

Tropical cloud radiative effects (CRE) are in deep convective regions determined by the relative proportions of thick, freshly detrained anvil clouds, and the thin anvils they evolve into. For thick anvil clouds, shortwave (SW) effects prevail over longwave (LW) effects, leading to a net climatic cooling effect. In contrast, LW effects prevail for thin anvil clouds with cloud optical depth (COD) smaller than 4, leading to a net warming effect (Berry & Mace, 2014; Hartmann & Berry, 2017; Kubar et al., 2007). Thick anvils occur adjacent to deep convective towers and form a reflective cold cloud shield. While most of the detrained ice that forms fresh

anvils is removed from the atmosphere within a few hours, thinning anvil clouds persist for much longer, often extending for hundreds of kilometers beyond the areas of active convection (Mapes & Houze, 1993; Mace et al., 2006; Protopapadaki et al., 2017). Any response of anvil cloud properties (e.g. occurrence, extent, or lifetime) to global warming could therefore lead to a significant radiative feedback.

The tropical troposphere is to first order controlled by an interplay between radiative cooling from the emission of thermal radiation by water vapor and latent heating in convective updrafts. The peak of convective detrainment therefore occurs just below the altitude where the radiative cooling becomes inefficient, at a temperature of about 220K. This relation will not change in a warmer climate with anvil clouds shifting to higher altitudes while remaining at a “fixed” temperature as proposed by the “fixed anvil temperature” (FAT) hypothesis (Hartmann & Larson, 2002). FAT has since been refined to take into account small cloud temperature changes associated with the presence of ozone, well-mixed greenhouse gases or changes in relative humidity (Harrop & Hartmann, 2012; Zelinka & Hartmann, 2010). It has been confirmed by cloud resolving model (CRM) and general circulation model (GCM) studies (Boucher et al., 2013; Harrop & Hartmann, 2016; Hartmann et al., 2019; Kuang & Hartmann, 2007; Zelinka et al., 2016), and satellite observations (Mace & Berry, 2017; Marvel et al., 2015; Norris et al., 2016; Zhou et al., 2014).

Several modeling studies showed a decrease in high cloud fraction with increased sea surface temperatures (SSTs) (Khairoutdinov & Emanuel, 2013; Tompkins & Craig, 1999; Zelinka & Hartmann, 2010). Bony et al. (2016) proposed a thermodynamic mechanism connecting the decrease in cloud fraction to increases in static stability. The mechanism involves FAT, static stability, and the reduction of convective outflow (and thus anvil cloud fraction) in a warmer world. The upper tropospheric static stability is bound to the moist adiabatic lapse rate. As the troposphere expands vertically, the decrease in pressure leads to an increased saturation specific humidity at a fixed temperature, which consequently warms the upper troposphere and increases its static stability (Hartmann et al., 2020; Zelinka & Hartmann, 2010). Consequently, based on the FAT hypothesis, a higher stability leads to a smaller convective detrainment, reducing the anvil cloud fraction and therefore limiting the tropical high cloud positive feedback.

Despite the arguments above that high cloud fraction should decrease in a warmer Earth, preliminary results from the Radiative-Convective Equilibrium Modeling Intercomparison Project show a large spread of modeled responses to increases in SSTs (Wing et al., 2020) including anvil cloud fraction changes. Moreover, various versions of the NICAM global and limited area CRM that represent convective cloud processes using fewer parameterizations than GCMs (and thus may be more realistic) show an increase in tropical high clouds with global warming (Ohno et al., 2019; Satoh et al., 2011; Tsushima et al., 2015). If the mechanism proposed by Bony et al. (2016) is present, an increase in high cloud fraction with warming simulated by some models implies that additional unknown feedbacks should play an important role. High clouds fraction increases with warming were shown to be connected to changes in deposition and ice crystal sedimentation, which were in turn driven by increases in upper tropospheric environmental relative humidity and radiative heating within cloudy parcels (Ohno & Satoh, 2018). Many of these processes are represented crudely in today's models, and Ohno et al. (2019) additionally pointed out the important role of turbulent mixing, which strongly depends on vertical grid spacing.

Several observational studies show that tropical outgoing longwave radiation (OLR) increases with surface warming more than predicted by the Planck response to warming (Choi et al., 2017; Lindzen & Choi, 2011). Lindzen et al. (2001) proposed a controversial hypothesis based on geostationary satellite observations, stating that the coverage of anvil clouds in the tropics will decrease with warming due to increased precipitation efficiency and consequent decreased convective detrainment, allowing a higher OLR. They named it the “Iris effect,” after the iris of the human eye, which expands in conditions of weak light to let more light pass, similarly to the putative tropical OLR response to the surface temperature in letting more OLR out in a warmer climate by reducing the high cloud cover. The Iris effect was proposed as a negative climate feedback, counteracting the greenhouse gas warming effect. The work was soon criticized for methodological reasons and lack of a clear physical mechanism (e.g. Fu et al., 2002; Hartmann & Michelsen, 2002). Howev-

er, the idea has recently gained more interest following the modeling study of Mauritsen and Stevens (2015) that implemented a temperature-dependent convective auto conversion rate, which resulted in a decreased climate sensitivity.

Hence, our understanding of tropical high clouds and the responses of their amount and optical depth to global warming are highly uncertain (Sherwood et al., 2020), sometimes leading to diametrically different conclusions. The role of specific microphysical processes, their interaction with radiation, and their changes due to surface warming and greenhouse gas increase are still unclear. This study's goal is to provide a better understanding of some of the processes controlling anvil cloud decay and their responses to global warming with the help of a Lagrangian approach in which we track air parcels detrained from regions of active deep convection. We show that the Lagrangian approach can, coupled to a high resolution model that is skillful in simulations of relevant climatic processes, reveal a process based view on the evolution of high clouds and their responses to global warming that is complementary to the standard climate model analysis.

1.1. Lagrangian Perspective on Anvil Evolution

Atmospheric models can be separated into two categories based on their treatment of fields' evolution related to the wind flow. Eulerian models treat the field evolution as a function of fixed space coordinates and time. In contrast, Lagrangian models describe fields following particles or air parcels along the flow. The Lagrangian perspective is particularly useful for studies of dynamic, quickly changing phenomena, giving a natural perspective on air parcel evolution. Lagrangian tracking of detrained clouds and water vapor has provided new insights into the lifecycle of tropical high clouds. For example, studies by Salathé and Hartmann (1997) and Soden (1998) highlighted the importance of the warming by large scale subsidence in decreasing the relative humidity of air masses detrained by deep convection. Soden et al. (2004) in addition showed that convection moistens the upper troposphere primarily by direct detrainment of water vapor, not through evaporation of anvil clouds. Luo and Rossow (2004) found that about 50% of tropical cirrus clouds originate from deep convection. Mace et al. (2006) used a combination of ground-based radar data with satellite feature tracking to show that tropical anvil cloud systems are long-lived with lifetimes of about 12 h. Gehlot and Quaas (2012) were the first to apply a similar tracking method on GCM model output to verify the model against observations and look at the changes in anvil cloud lifecycle in a simulation with increased SSTs. The Lagrangian analysis suggested that a combination of increased cloud fraction and cloud altitude was the driving force behind a positive cloud feedback, despite increases in cloud albedo. Jensen et al. (2018) followed trajectories of ice crystals detrained from a mid-latitude thunderstorm driven by a CRM simulation. They simulated the first 3 h of the microphysical evolution of detrained ice crystals and showed the large importance of gravitational settling and depositional growth for the anvil evolution. So far, three-dimensional Lagrangian tracking has never been applied to studies focusing on deep convective outflow and the transition between deep cumulus to thick and thin anvil clouds. The tracking of detrained air parcels allows us to determine the lifetime of anvil clouds and estimate sources and sinks of ice during the cloud evolution and their changes with global warming.

The study focuses on the region between 130°–180°E and 20°S–20°N, which we call Tropical Western Pacific (TWP) and is typical of regions with warm and uniform SST and frequent deep convection. Only anvil clouds that originate from maritime deep convective cores are considered as the continental/island deep convection is controlled by different processes and is less important for the tropical radiation balance. Section 2 introduces the satellite and model data used and describes the details of the used mesoscale convective system (MCS) tracking and air parcel tracking methods. Section 3.1 briefly assesses the model performance in the TWP. The Lagrangian perspective on the simulated anvil cloud evolution in present climate is presented in Section 3.2. Mean climate responses to warming are presented in Section 4.1, followed by a description of MCS responses to global warming in Section 4.2. Finally, Section 4.3 presents changes of anvil properties along detrained trajectories due to global warming and their radiative implications. A discussion on the implications and limitations of the model simulations is provided in Section 5. Conclusions are given in Section 6.

2. Methods

2.1. Model

We use the Exascale Earth System model (E3SM), a new GCM developed by the US Department of Energy (Golaz et al., 2019). The model consists of interacting components simulating atmosphere, land surface, ocean, sea ice and rivers. The atmospheric component of E3SM (Rasch et al., 2019) is a descendant of the CAM5 model (Neale et al., 2012), including new ways of coding, improved model performance, increased resolution, and numerous additional physical parameterizations related to clouds and aerosols. The model uses a spectral finite element dynamical core (Dennis et al., 2012) with 72 vertical layers. The upper tropospheric resolution of about 500 m is significantly higher than most state-of-art GCMs, and allows for a more realistic representation of upper tropospheric clouds. E3SM performs well compared to other CMIP5 models (Golaz et al., 2019), despite known model biases (Xie et al., 2018; Y. Zhang et al., 2019). In particular, the model underpredicts clouds in the tropical warm pool area by about 10%–20%, which was found to be related to the increase of the vertical resolution from 30 to 72 layers (Xie et al., 2018).

We use the high resolution (about 0.25°) version of the model (Caldwell et al., 2019), in which the large tropical MCS are better resolved. The phrase “MCS” in this publication does not imply that the simulated convective systems have all of the characteristics of the observed MCS (e.g. Houze, 2004), even if the shown simulated properties match the observations. E3SM uses a convective parameterization by G. J. Zhang and McFarlane (1995) with the dilute plume closure by Neale et al. (2008). Turbulence, shallow convection and cloud macrophysics are simulated by the third order turbulence closure Cloud Layers Unified By Binormals (CLUBB) parameterization (J. C. Golaz et al., 2002; Larson & Golaz, 2005). The model uses an updated version of Morrison and Gettelman (2008)’s scheme for stratiform cloud microphysics (Gettelman & Morrison, 2015) and is coupled with the RRTMG radiative transfer model (Iacono et al., 2008; Mlawer et al., 1997). The COSP version 1.4 satellite simulator (Bodas-Salcedo et al., 2011) is run in parallel to the model. The atmospheric component of the model was coupled with the land model only, using prescribed SSTs.

2.2. Simulations

We perform two simulations representing present day climate (REF, climREF, see also in Table 1) and two simulations representing a possible warmer future climate state (4K, clim4K). SSTs and sea ice extent were prescribed using a monthly present-day climatology (simulations REF, climREF) based on the Smith/Reynolds EOF data set (Hurrell et al., 2008). Simulations 4 K and clim4K use the same SST pattern assuming a uniform 4K warming. The simulations used for calculation of the mean climatic properties and cloud feedbacks with monthly output frequency (climREF and clim4K) were run for only 3 years due to the large computational expense.

The simulations REF, NUDGE, and 4K, used for both MCS tracking and trajectory calculations last 3 months (Jun 1–Aug 31) with a 8 days spin-up period (May 24–May 31) that is not considered in the analysis (Table 1). Because many fields were archived hourly for subsequent analysis, longer simulations were not possible due to storage space limitations. The NUDGE simulation uses a linear interpolation nudging technique developed by Sun et al. (2019). The model horizontal wind fields were nudged at every model time step to an interpolated value based on six hourly ERA-Interim reanalysis data (Dee

Table 1
A List of Performed Simulations

Simulation	Length	Output frequency	Description
NUDGE	3 months	1 h	Winds nudged to reanalysis data, SSTs from 2016
REF	3 months	1 h	Free running experiment with climatologic SSTs
4K	3 months	1 h	Same as REF but with SSTs increased by 4K
climREF	3 years	1 month	Same as REF, but initialized in January
clim4K	3 years	1 month	Same as 4K, but initialized in January

et al., 2011), with a relaxation timescale of 6 h. The simulation NUDGE uses monthly mean SSTs for the months of June–August 2016 from the same data set for a better comparison with MCS observations from the same period.

In addition we estimate cloud feedbacks based on Zelinka et al. (2016), which uses cloud radiative kernels (Zelinka et al., 2012a) and output from the ISCCP satellite simulator (Klein & Jakob, 1999; Webb et al., 2001) separated into cloud top pressure and COD bins. The feedback calculation allows one to separately account for the contribution of changes in cloud altitude, cloud amount, and cloud optical depth to the total cloud feedback. We calculate both the cloud feedback of all clouds as well as the cloud feedback for clouds with cloud top pressures smaller than 440 hPa.

2.3. CERES Satellite Data

We use the CERES-derived top-of-atmosphere radiative fluxes (Wielicki et al., 1996) from the CALIPSO-CloudSat-CERES-MODIS (CCCM) data set (Kato et al., 2011) for the months of June–August 2007–2010 in the TWP (20°S to 20°N, 130° to 180°E). The horizontal resolution of CERES pixel data is approximately 30 km. To avoid problems at large solar zenith angles, we limit the analysis to CERES pixels for which the solar zenith angle and the CERES viewing angle zenith are smaller than 40°. Given that the data in the CCCM data set are collocated with the CloudSat-CALIPSO radar-LIDAR measurements, that limits the observations to the 1.30 p.m. (afternoon) overpass of the A-Train satellite constellation.

2.4. Geostationary Satellite Data

We use the Himawari-8 geostationary satellite observations (Bessho et al., 2016) of brightness temperature (BT) at the infrared channel (11.2 μm) between 1 June–31 August 2016. The downloaded Himawari data product only includes every fourth pixel and scan line, making the effective horizontal resolution about 8 km at nadir and 12 km at the edge of the study domain. These data were subsequently regridded to 0.25° (about 25 km) to match the model output. Regridded pixels were computed by averaging the native grid pixels within the new grid boundaries. The data sets' temporal resolution of 1 h allows individual MCS to be tracked throughout their lifecycle.

2.5. Lagrangian Methods

Our work largely relies on two distinct tracking methods: MCS tracking, based on Himawari BT measurements, and the three dimensional air parcel tracking, based on the resolved model wind fields. The MCS tracking follows the parent deep convective system throughout all stages of its evolution, from the convective initiation to its decay, providing a good overview of the convective processes and the adjacent thick anvil clouds, while missing the decaying thin anvil clouds.

In contrast, the air parcel tracking follows cloudy parcels as they leave the MCS region and become thin cirrus. It is initialized at the point of maximum MCS activity as determined by the MCS tracking algorithm. Air parcel tracking provides an estimate of the decay timescale of an anvil cloud, following its evolution from a fresh thick anvil to a thin cirrus cloud, and provides a detailed understanding of the evolution of cloud processes. A more detailed description of each tracking mechanism, their strengths, and weaknesses can be found in the Sections 2.5.1 and 2.5.2. The animation of a 2 week long segment of the simulation provides an intuitive view of both tracking mechanisms (Movie S1).

2.5.1. Mesoscale Convective System Tracking

We apply an MCS tracking algorithm to the 11.2 μm BT measurements from the Himawari and to the 10.5 μm simulated BT retrieval using the COSP satellite simulator. The small difference in the BT wavelength of the two channels does not affect our findings. Both Himawari and E3SM data are tracked in 1 h intervals, enabling an accurate MCS tracking. The tracking algorithm is based on Fiolleau and Roca (2013) and is described in detail in Wall et al. (2018). It consists of two steps:

Table 2
Tracked MCS properties

	Himawari	NUDGE	REF	4K
1. Fixed BT				
BT limit (K)	210–240	210–240	210–240	210–240
MCS number	1762	1,243	853	1,354
Lifetime (h)	12.7 ± 5.4 (11)	18.8 ± 6.1 (18)	16.9 ± 5.4 (16)	15.9 ± 5.4 (15)
Equiv. Diameter (km)	247 ± 97 (223)	260 ± 75 (248)	267 ± 68 (257)	264 ± 81 (250)
2. Percentile based BT				
BT limit (K)	201.4–238.1	209.9–236.7	213.5–239.3	209.0–237.3
MCS number	794	1,234	1,285	1,178
Lifetime [h]	14.5 ± 5.0 (13.5)	17.9 ± 6.0 (17.0)	16.2 ± 6.0 (15.0)	15.6 ± 5.4 (15.0)
Equiv. Diameter (km)	302 ± 90 (290)	247 ± 73 (235)	248 ± 69 (237)	260 ± 80 (246)

The numbers represent mean values with the respective standard deviations. The median values are in brackets.

1. Detection step: The cold core is detected based on the BT threshold (between 200K and 214K depending on the specific case, see Table 2). The cold core must cover at least 17 pixels and last for at least 2 h to be considered by the algorithm
2. Spreading step: The cold cloud shield is incrementally increased from the BT threshold to the warm limit in both space and time (ranging between 235K and 240K as listed in Table 2)

The tracking algorithm is able to track MCS throughout their lifecycle, from the growth to the decay stage (Wall et al., 2018). However, once the clouds become optically thinner, the BT signal of cold clouds is mixed with the signal from warmer, lower lying levels. The algorithm reliably tracks upper tropospheric clouds to the warm BT limit of 235K–240K, which corresponds to a COD of about 3–10. The tracking algorithm therefore cannot account for the thin anvil clouds that spread beyond the region detected by the cloud mask. The altitude of cloud top does not change by more than 1 km within the tracked region as suggested by the Figure 6a and confirmed in other studies (Bouniol et al., 2016; Sokol & Hartmann, 2020). An example of the cold cloud shield output of the tracking algorithm is shown in Figures 1b and 1c. The blue and green contours outline the limits of the detected cold cloud shield which we take as the MCS boundaries. The green contoured MCSs are removed from the analysis as they either cross land at some point in their lifetime or touch the domain boundaries. The MCS lifetime is defined as the time between the first and last detection of an MCS based on the cold cloud shield. No merge or split events are allowed, as the algorithm partitions the cold cloud shield on the basis of proximity to the cold cores.

We use two separate ways of setting the BT threshold for tracking the MCS. The first method relies on fixed BT thresholds of 210K for cold core detection and 240K for the warmest contours that are tracked as part of the cold cloud shield (see Wall et al., 2018 for details). However, fixed BT thresholds propagate mean climatic errors into the object-oriented MCS tracking analysis. Those errors will be discussed below in the evaluation of BT PDFs in Figure 3. The work by Rempel et al. (2017) and Senf et al. (2018) suggests that it can also be useful to apply a BT correction before the object-based MCS tracking analysis, so we therefore also use a prescribed lower and upper BT percentile to define the cold cloud shield used to track the detection and spread of cold cloud shield area instead of a fixed BT limit. A percentile-based metric also helps estimating the impacts of global warming driven changes of MCS properties and the anvil cloud evolution, as described in Sections 4.2 and 4.3. Similar percentile based comparison metrics are frequently used in studies of extreme precipitation responses to global warming (Fischer & Knutti, 2015, 2016; Pendergrass & Knutti, 2018).

We chose the 0.4 and 8.15 BT percentiles as the cold core detection limit and the upper BT limit, which correspond to the BT values of 200K and 235K in the full resolution Himawari data set for consistency with the work by Wall et al. (2018). The chosen lower percentile limit corresponds to a BT of 201.4K in the regridded

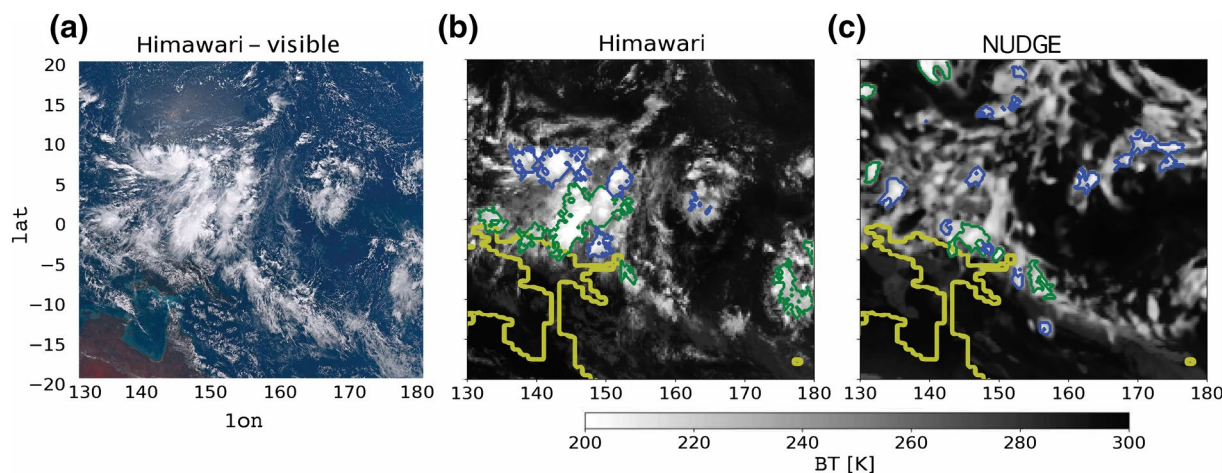


Figure 1. A snapshot of the region of interest for July 2 at 2.00 UTC. (a) Visible Himawari satellite image; (b) the equivalent BT measurement; (c) the NUDGE model simulation at the same time step. Blue contours represent tracked MCSs, green contours represent MCSs that are tracked but removed from the analysis as they touch the edge of the domain or land. Yellow contours represent boundaries of land masses. MCSs, mesoscale convective systems; UTC, coordinated universal time.

Himawari data set used in this analysis, to 210K in the nudged, and 213.5K in the free running E3SM model simulation as stated in Table 2. The reasons for the large modeled BT bias are described in Section 3.1.2.

2.5.2. Lagrangian Analysis of Anvil Clouds

1. Determination of trajectory starting locations: High frequency (1 h) model output from June 1 to August 31 from simulations REF and 4K is used for calculating forward trajectories. The forward trajectory calculation is designed to monitor and capture the decay of anvil clouds from their early thick stage until dissipation as thin cirrus. Monitoring starts at the peak of MCS convective activity, defined as the point in the MCS evolution when the detected cold cloud shield occupies the largest area (Roca et al., 2017). At this point the model columns covered by the cold cloud shield (blue contours in Figure 1) are selected to determine the right vertical launch level for the trajectories. The vertical launch level is chosen to be the first model level from the model top downward to have an ice mixing ratio (QI) larger than $3 \times 10^{-5} \text{ kg kg}^{-1}$ and a detrainment tendency from the parameterized convective updrafts larger than $10^{-9} \text{ kg kg}^{-1} \text{ s}^{-1}$. Launch levels are limited to temperatures colder than -35°C , as the study is focused on cold portions of anvil clouds.
2. Trajectory calculation: Trajectories are computed in a post processing step with the Lagrangian Analysis Tool (LAGRANTO, Sprenger & Wernli, 2015; Wernli & Davies, 1997). Trajectories are computed forward in time for 40 h. Microphysical and radiative quantities are traced by identifying the value of those quantities from an archived model data set followed by a bilinear interpolation of the neighboring grid values in the horizontal dimension (latitude, longitude) and a linear interpolation in the vertical dimension (model level, Sprenger & Wernli, 2015). This tracking uses resolved three dimensional wind fields that allows us to track the changing microphysical and radiative properties after detrainment. The analysis neglects snow particles due to their larger sedimentation velocity that leads to a rapid removal from the atmosphere and therefore a smaller climatic influence compared to the longer lived detrained ice crystals.

In a second post processing step we remove the trajectories that encountered a subsequent significant episode of detrained ice (i.e. detrainment larger than $0.3 \times 10^{-9} \text{ kg kg}^{-1} \text{ s}^{-1}$) after the initial 4 h of the development. This allows us to study cloud decay of anvils that are not influenced by new occurrence of convection. The additional criterion reduces the number of selected trajectories by 35%, from a total number of 190,000 to about 125,000, while not affecting the main conclusions of our study. We define a trajectory as containing “ice cloud” if the local cloud fraction (output field CLOUD) exceeds 10% and at the same time QI exceeds 0.1 mg kg^{-1} . The QI limit was chosen to be close to the minimum detection limit by CALIOP LIDAR, roughly corresponding to COD of 0.01 (Avery et al., 2012). The anvil cloud lifetime is defined as the point

in time when the fraction of trajectories containing cloud decreases below 50%. Note that the total column cloud fraction could still be large as air parcels containing ice can be detrained from multiple levels below and above the tracked one. Due to lateral mixing the cloud properties along trajectories in the later stage of anvil evolution represent a mix of air from anvil and nonanvil air masses. We omit the radiatively active and prognostic snow from the trajectory analysis due to its larger sedimentation velocity compared to cloud ice (X. Zhao et al., 2017) and storage space limitations. The vertical component of the trajectory calculation does not include the convective mass flux term as that contribution is small compared to the grid box average updraft velocity.

3. Results: Present Climate

3.1. Model Evaluation

3.1.1. Mean Climate in the Tropical Western Pacific

Figure 2 shows the probability density function (PDF) of OLR-albedo pairings observed by CERES for the months of June–August, similarly to Figure 2 in Hartmann and Berry (2017), and the equivalent fields simulated by the model. The model output is limited to grid boxes with insolation values exceeding 1000 W m^{-2} , which approximately corresponds to the zenith angle limit of 40° used to filter the CERES data. The general shape of the histogram describes the evolution of anvil clouds: their lifecycle begins in very reflective deep convective cores at low OLR and high albedo values. The detrained anvil clouds gradually thin, decrease their albedo, and allow more OLR to escape to space until reaching the modal point of the distribution at albedo values of about 0.08 and OLR of $270-290 \text{ W m}^{-2}$ which corresponds to nearly clear sky conditions. The model is able to reproduce the general shape of the distribution and therefore anvil decay remarkably well, with the exception of the missing highest albedo and lowest OLR points and a minor albedo overestimation at OLR values between 200 and 300 W m^{-2} . E3SM therefore shows good skill in simulating the process of anvil thinning, that is on one hand crucial for the radiative balance of tropical deep convective regions, while on the other hand traditionally challenging for GCMs to correctly simulate (Wall & Hartmann, 2018).

3.1.2. Mesoscale Convective Systems

Figure 3 shows the PDF of BT in the Tropical Western Pacific region observed by Himawari and modeled by E3SM with the help of a satellite simulator. We focus for now on the NUDGE and REF simulations and refer back to the figures to examine climate change effects in the 4K simulation only in Section 4. The Himawari distribution sharply peaks at about 295K, while the nudged and free running model simulations show a peak at a few K warmer temperatures. This BT peak corresponds to clear sky regions, clear sky regions with thin cirrus clouds, or regions covered by low clouds. The simulated warm bias in BT peak is likely caused

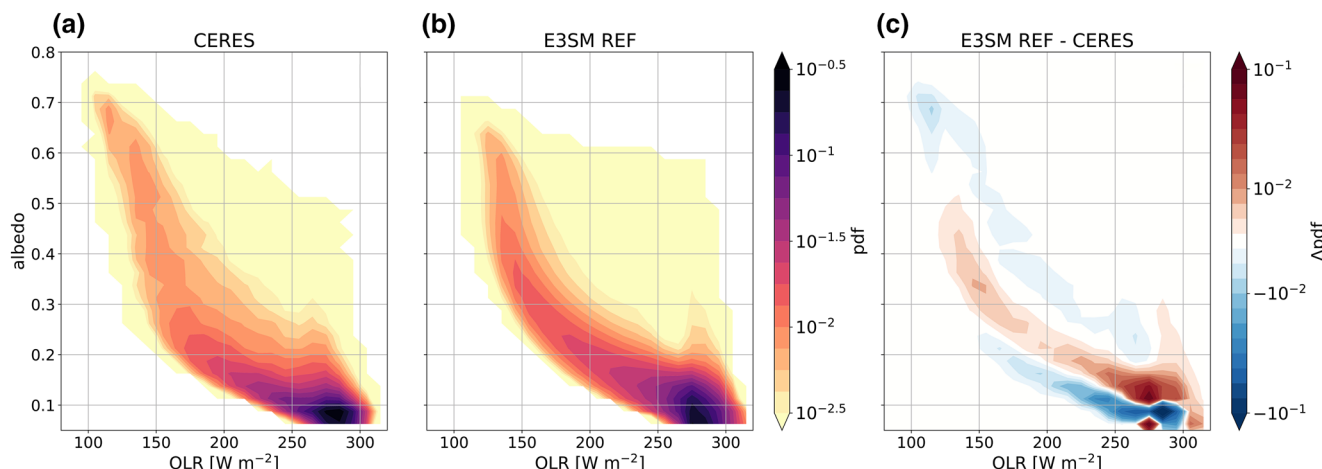


Figure 2. Albedo-OLR histogram for the Tropical Western Pacific from 4 years of CERES radiative flux observations for months June–August (a), the equivalent from the REF model simulation (b), and the anomalies between the two (c). OLR, outgoing longwave radiation.

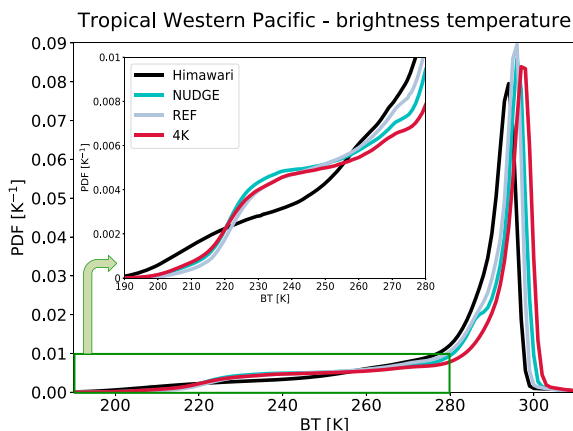


Figure 3. BT histogram for the Tropical Western Pacific in JJA 2016 from Himawari observations and model simulations. BT, brightness temperature.

comparing BT snapshots in Figure 1b and 1c. Moreover, despite efforts to evaluate the fields at the same nominal resolution, the model lacks the fine structures observed by Himawari. This is not surprising, as the effective model resolution is about 3–4 times larger than a single gridbox cell for the spectral element dynamical core used here.

When MCS are defined using fixed BT thresholds, the model underestimates the number of MCS and overestimates their lifetime (Table 2 and Figures 4a and 4c), while simulating MCS of comparable size. The maximum MCS equivalent diameter is close to 250 km in both Himawari and E3SM. The MCS mean lifetime from Himawari observations is found to be 12.7 h, which is comparable to Wall et al. (2018). The simulated MCS are more persistent, with average lifetimes of 19 h (NUUDGE) and 17 h (REF). The excessive lifetime of the model clouds can at least in part be attributed to a series of parameterization choices made in the development of the atmospheric component of E3SM (Rasch et al., 2019). The effective radius of ice crystals detrained from deep convection was set to 12 μm , which is smaller compared to observations (Van Diedenhoven et al., 2016), in order to increase the amount of cloud ice in the atmosphere (Xie et al., 2018). This choice, in conjunction with a decision to use the Meyers et al. (1992) ice nucleation parameterization (known to produce unrealistically high nucleation rates) in the high resolution version of E3SM (Caldwell et al., 2019) produces too many ice crystals that consequently remain small during vapor deposition. Finally, as mentioned in the previous subsection, the effective model resolution is larger than its nominal resolution. Regridding the Himawari observations to 0.5 and 1° increases the MCS lifetime for 1 and 2 h, respectively, explaining part of the model bias.

Results using the percentile based masking give a different perspective on simulated MCSs: in this case the model overestimates the MCS number but underestimates the cold cloud shield area, with a comparable MCS lifetime (Figures 4b and 4d). This is expected, as the percentile-based BT MCS detection threshold of 201.4K for Himawari observations is significantly lower than 209K–213.5K for the model simulations. MCS with colder BT indicate a stronger convective activity with higher and colder cloud tops. The higher convective activity is also connected to a longer MCS lifetime and larger MCS cold cloud shield area (Machado et al., 1998; Protopapadaki et al., 2017; Strandgren, 2018).

Figure 5 shows the diurnal cycle of the number of MCS at peak extent in each of the 3-hourly bins. The peak MCS extent was previously shown to correlate with the peak in convective activity and with the lowest BT that is achieved in the course of an MCS lifecycle (Roca et al., 2017). When using a BT threshold of 210K for the detection of cold cores, the observations show a double peak in MCS activity: the first peak occurs in early morning hours (3–5 local time), the second peak occurs in the afternoon hours (15–17 local time). However, when using the colder percentile-based BT threshold for the detection of cold convective cores, the afternoon peak disappears. This result is consistent with Nesbitt and Zipser (2003) that showed an early

by the underprediction of thin low clouds (Y. Zhang et al., 2019). The observed and simulated distributions are negatively skewed with a long tail extending down to 190K. BT values colder than 240K correspond to cold cloud tops; we define such gridboxes as cold cloud fraction. These BT values include deep convective cores and anvil clouds of visible COD greater than about 5, and do not include thin anvil cloud and other in-situ formed cirrus clouds. E3SM simulates a cold cloud fraction of 9.7% in the nudged simulation (NUUDGE) and 8.5% in the free running simulation (REF). This is close to the observed value of 9.8 %. The model substantially underestimates the occurrence frequencies of BT colder than 220K (represented by the highest albedo and lowest OLR values in Figure 2), and overestimates BT in the range between 225K and 250K. This is a signal of a too low (and consequently too warm) cloud top, caused by a deep convective detrainment level bias and the underestimation of the strongest overshooting convective cores, as already noted by Y. Zhang et al. (2019). The bias, which existed in the predecessor model CAM5 (Wang & Zhang, 2018), has not been solved in the E3SM model, in spite of increased vertical resolution and efforts to address the bias through tuning (Xie et al., 2018). Qualitatively the biases are also visible by

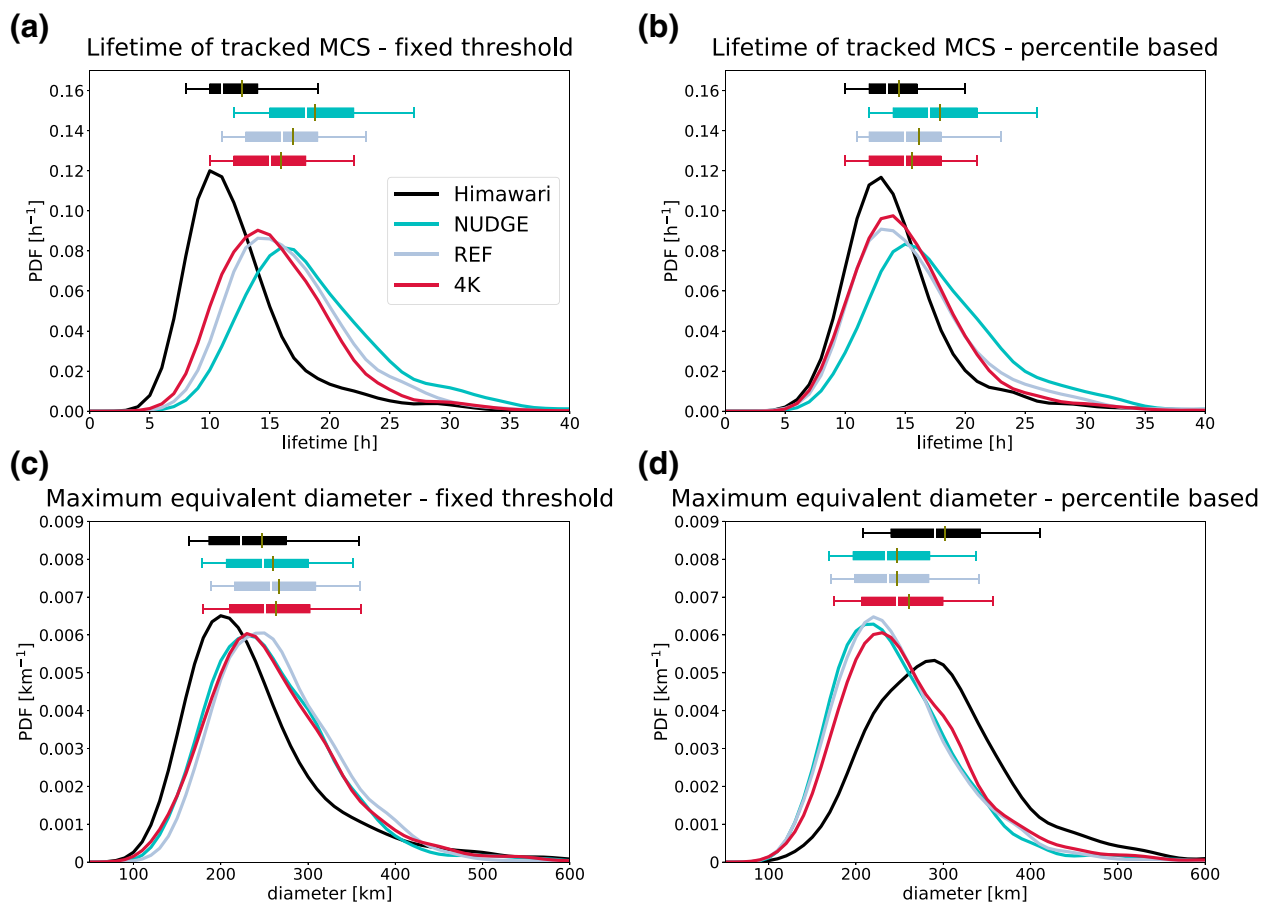


Figure 4. Lifetime and maximum diameter distribution of tracked MCS. The boxplot area is shaded between the 25th and 75th percentiles, while its whiskers represent the 10th and 90th percentiles. The olive lines represent the mean values of the distributions. MCS, mesoscale convective system.

morning peak in MCS activity, followed by a weaker afternoon peak of warmer BT features representing weaker deep convection. The model simulates a similar double peak in MCS activity when using the fixed 210K cold core detection threshold in both the REF and NUDGE simulation. The percentile based model results still show the secondary afternoon peak, which is not surprising, given that the percentile based cold core detection threshold does not change much from a fixed threshold of 210K.

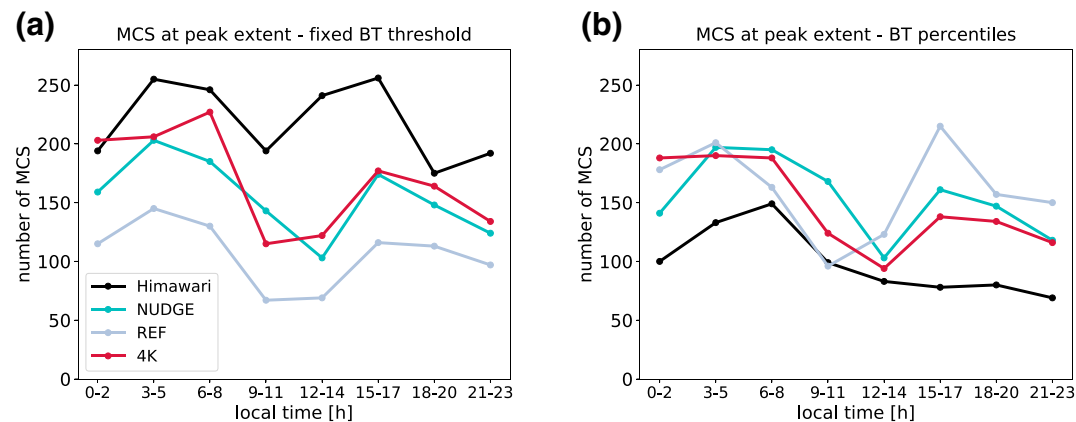


Figure 5. Diurnal cycle of peak MCS extent for (a) the fixed BT threshold and (b) the percentile based BT threshold. BT, brightness temperature; MCS, mesoscale convective system.

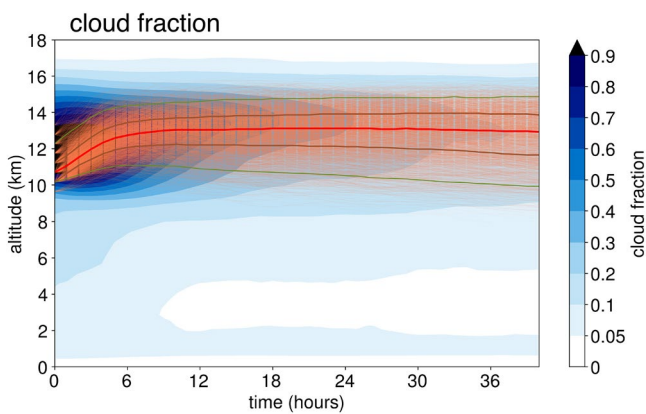


Figure 6. Altitude of a random sample of 5,000 trajectories (in orange) as a function of time after the launch of trajectories. Plotted in the background is the mean cloud fraction in columns containing trajectories. The red line represents the median trajectory altitude, the brown lines the 25th and 75th percentile values, the green lines 5th and 95th percentile values.

In summary, the model can reproduce the simulated cold cloud fraction despite some biases in the simulation of MCS evolution, which originate from the underestimation of the coldest BT. The performance of the model in simulating large tropical MCS is satisfactory, given the use of convective parameterization and a resolution of $0.25 \times 0.25^\circ$, which is barely able to dynamically resolve MCS. For a more extended evaluation of E3SM using traditional evaluation metrics, the reader is referred to Caldwell et al. (2019), Rasch et al. (2019), Xie et al. (2018), and Y. Zhang et al. (2019).

3.2. A Lagrangian Perspective on Anvil Cloud Evolution

Figure 6 displays the cloud fraction in the vertical column at the trajectory location following air parcels from the tops of deep convective clouds. The trajectory launching points occur at different altitudes, ranging from 10 to 13 km, with a median elevation of about 11 km. The trajectories start in regions of active convection with resolved vertical winds that are strong enough to loft the detrained air parcels and ice for about 2 km within the first 5–8 h after the trajectory is initialized. After the initial ascent the trajectories remain at roughly constant altitude. The trajectories follow the upper tropospheric peak in cloud fraction that represents

gradually thinner anvil clouds. The convective scheme is not only detraining condensed water but also vapor, which enhances the humidity in the detrained layers for at least 40 h after the initial convective event. The relative humidity with respect to ice on average exceeds 100% near areas of active detrainment, and is maintained at values beyond 70% in the MCS outflow in the tropical tropopause layer between 14 and 17 km altitude (not shown). The increased relative humidity in the convective outflow layer offers an alternative explanation for an anvil cloud fraction maximum near the trajectory altitude, given the dependence of the cloud fraction scheme to the total humidity that includes specific humidity contributions from both vapor and ice condensate (Gettelman et al., 2010).

Figure 7 shows the gradually decreasing fraction of cloud-containing trajectories, reaching 50% about 15 h after detrainment. We separate the anvil evolution in three stages: thick ($QI > 30 \text{ mg kg}^{-1}$), intermediate ($30 \text{ mg kg}^{-1} > QI > 3 \text{ mg kg}^{-1}$), and thin ($QI < 3 \text{ mg kg}^{-1}$). Thick anvils quickly decay within the first 3–4 h, intermediately thick anvils dominate the cloud distribution between hour 4–10, and thin anvil clouds are dominant about 10 h after the trajectories are initialized. A cloud decay sensitivity test that considers all calculated trajectories, including those that encounter significant detrainment events after the first 4 h of the evolution is shown in Figure S1.

A sensitivity study using different minimum QI and cloud fraction limits can be found in Figure S2 and is described in Text S1.

3.2.1. Lagrangian Anvil Cloud Ice Mass Balance

We present the dominant sources and sinks of ice during the evolution of the anvil cloud from its thick (hour 0–4) to thin stage (hour 10 and beyond) using trajectories. The trajectories start at locations with QI median values of about 55 mg kg^{-1} , decreasing to below 5 mg kg^{-1} over the course of the first 10 h of the cloud evolution (Figure 8a). The median in-cloud ice crystal number decreases with evolution from about $4,000 \text{ g}^{-1}$ (or about 800 L^{-1} at the detrainment level) to $1,000 \text{ g}^{-1}$ (Figure 8d). The ice crystal number subsequently decreases to about 300 g^{-1} (approximately 60 L^{-1}) at hour 20. The ice crystals initially grow slightly from 32 to 35 μm , and rapidly decrease in size until reaching a plateau at 15–20 μm between hour 5 and 15 of the evolution, after which the size decreases again, reaching about 5 μm at hour 20 (Figure 8c).

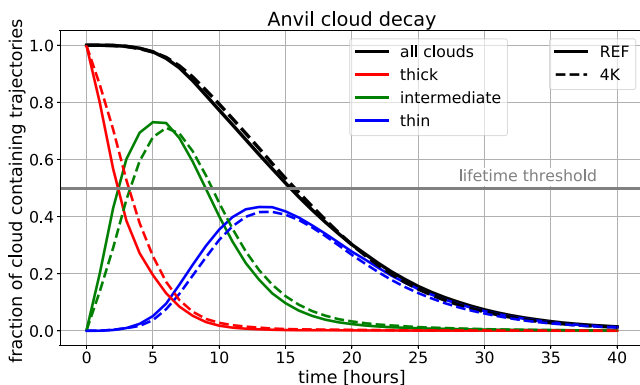


Figure 7. Fraction of trajectories that are containing a cloud for REF and 4K simulations (in black), divided into thin ($QI < 3 \text{ mg kg}^{-1}$), intermediate ($30 \text{ mg kg}^{-1} > QI > 3 \text{ mg kg}^{-1}$), and thick ($QI > 30 \text{ mg kg}^{-1}$) categories (in red, green, and blue, respectively). The sum of the three cloud categories is equal to the “all clouds” line. QI, ice mixing ratio.

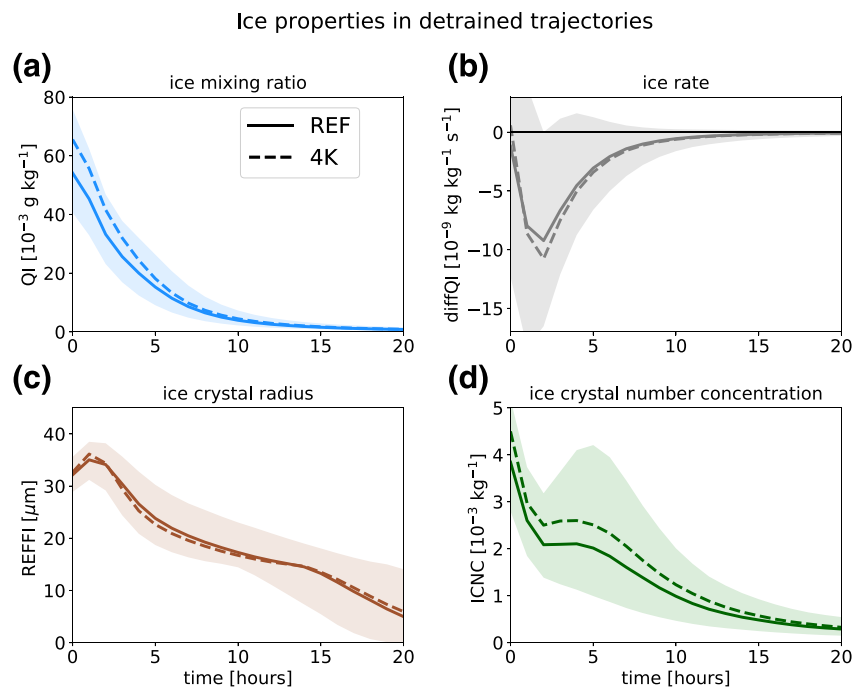


Figure 8. Median in-cloud ice mixing ratio (QI) (a), ice rate (diffQI) calculated as $\frac{QI_{t+1} - QI_t}{dt}$ (b), in-cloud ice crystal effective radius (REFFI) (c), and in-cloud ice crystal number concentration (ICNC) (d) in detrained trajectories. Ice rate is defined as the sum of all ice sources and sinks of ice plotted separately in Figure 9. Shaded area represents the spread between the 25th and 75th percentile values for REF.

The net water vapor deposition (which includes both growth by deposition and shrinking by sublimation) is the dominant source of ice over the whole anvil cloud lifetime (Figure 9). The net deposition is particularly large initially as most of the trajectories are supersaturated with respect to ice, supporting ice crystal growth (not shown). The direct detrainment of ice mass (with an assumed effective ice radius of 12 μm)

from the convective cores represented by the convective parameterization is an important source of ice in the first 2 h of the anvil evolution, indicating the presence of active deep convection. Despite focusing on trajectories at temperatures colder or near the homogeneous freezing temperature of water, the growth of ice crystals at the expense of water droplets (Bergeron-Findeisen process) cannot be fully neglected in the first 5 h of the evolution as some of the trajectories experience temperatures near -35°C where part of the detrainied condensate is in liquid form. Finally, the contribution of new ice crystal nucleation to the ice mass tendency is generally negligible and is therefore omitted from Figure 9. On the other hand, snow formation via ice crystal aggregation is the dominant sink of ice throughout the full lifecycle of anvil clouds. Aggregation moves ice crystals that cross the temperature dependent threshold size to snow and therefore increases with the growth of ice crystals. Accretion is the removal of ice crystals by collisions with snowflakes and is an important sink of ice in the precipitating stage of the anvil cloud, i.e. in the first 5 h of the anvil evolution, after which it becomes negligible, due to absence of snow particles in thin anvil clouds. Interestingly, ice crystal sedimentation is only of secondary importance compared to aggregation even in the thin anvil stage, beyond hour 10 of the trajectories.

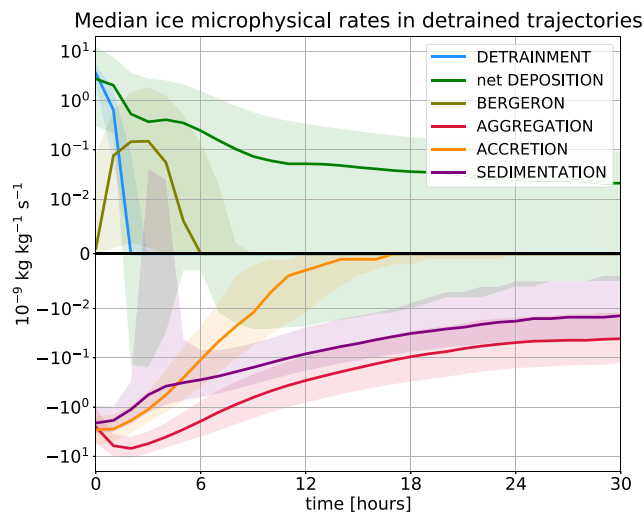


Figure 9. Lagrangian mass budget along trajectories containing ice cloud during the first 30 h of evolution from the REF simulation. The shaded area represents the spread between the 25th and 75th percentile values.

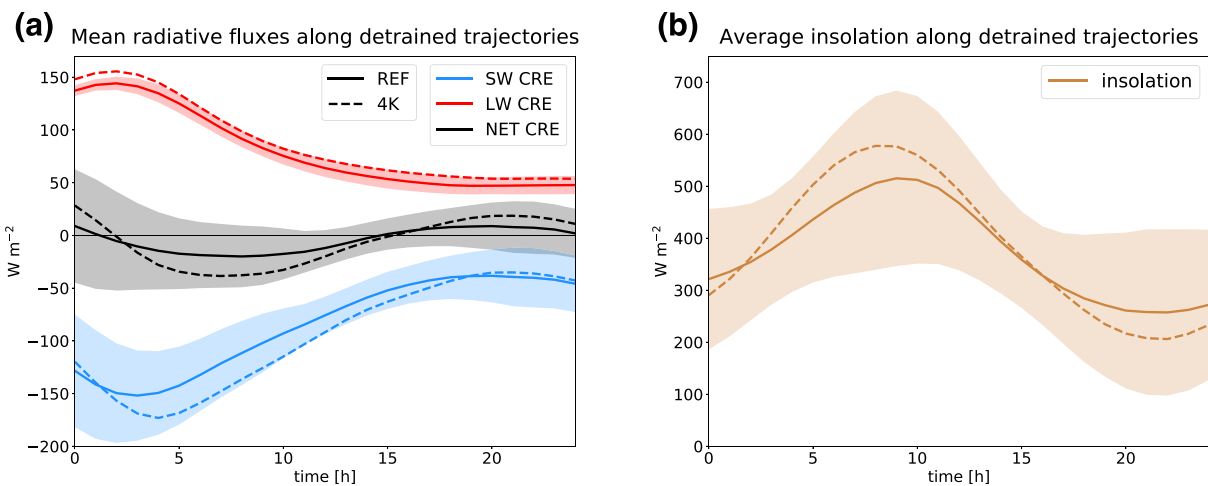


Figure 10. (a) CRE along detrained trajectories for the two simulations. Shaded area represent one standard deviation for REF. (b) Mean insolation values along tracked trajectories for the two simulations. Shaded area represent one standard deviation for REF.

Table 3

Mean Changes in Cloud Radiative Effects (CRE) Along Trajectories Averaged During the First 24 h

	REF	4K-REF	4K-REF ConstInsol
LW CRE (W m^{-2})	81.0	8.2	8.2
SW CRE (W m^{-2})	-85.4	-10.3	-4.1
NET CRE (W m^{-2})	-4.4	-2.2	4.1
NET feedback ($\text{W m}^{-2} \text{ K}^{-1}$)	-	0.5	1.0

The SWCRE is in the last column calculated using a constant insolation value of 390 W m^{-2} instead of the model simulated insolation.

3.2.2. Radiative Evolution

Anvil ice microphysical properties are tightly related to the radiative effects and climatic effects of anvil clouds. Freshly detrained thick anvil clouds that contain large QI are very reflective to visible radiation and have therefore a large shortwave cloud radiative effect (SWCRE). They also effectively prevent LW radiation from escaping to space from lower lying, warmer layers of the atmosphere, resulting in a large LWCRE. Interestingly, the averaged radiative effects along the trajectories start with a positive net CRE, which gradually decreases in the first 5 h of the anvil evolution (Figure 10a), despite decreasing QI, ice crystal number, and consequently cloud albedo. This can be explained by the average insolation that the tracked clouds receive over the course of their lifetime (Figure 10b). The mean insolation starts at values of about 300 W m^{-2} , increasing to 500 W m^{-2} at hour 10. The peak in MCS activity, where

trajectories start, on average occurs during early morning hours just before sunrise (Figure 5b). Within a few hours, most of the trajectories are exposed to higher insolation values near mid-day, leading therefore to a larger SWCRE causing the net CRE to shift to negative values (Figures 10a and 10b). At this point, both SWCRE and LWCRE start decaying significantly. The averaged CRE along trajectories for 24 h of cloud evolution exceed values of 80 W m^{-2} in terms of LWCRE and SWCRE, with a small negative net CRE term (Table 3). These results are not very sensitive to the trajectory selection criterion, as shown by computing radiative fluxes along all computed trajectories (Table S1).

4. Results: Future Climate

4.1. Mean Climate Responses to Warming

We first evaluate mean climate responses to warming for the Tropical Western Pacific. The model simulates a 40% increase in precipitable water and a 20% increase in liquid water path for the clim4K simulation (not shown) with very little change in relative humidity (Figure 11f). QI increases significantly with global warming (Figure 11g) at all temperatures, particularly in the 230K–250K range and is discussed in Section 5.1. Interestingly, cloud liquid decreases in the boundary layer but increases near the melting layer, possibly due to increased melting of ice (Figure 11d). The peak in anvil cloud amount remains at temperatures between 220K and 212K in both simulations (Figures 11a). The anvil cloud fraction decreases with warming, which is consistent with a decrease in the upward mass flux by the convective scheme (Figure 11c). In contrast

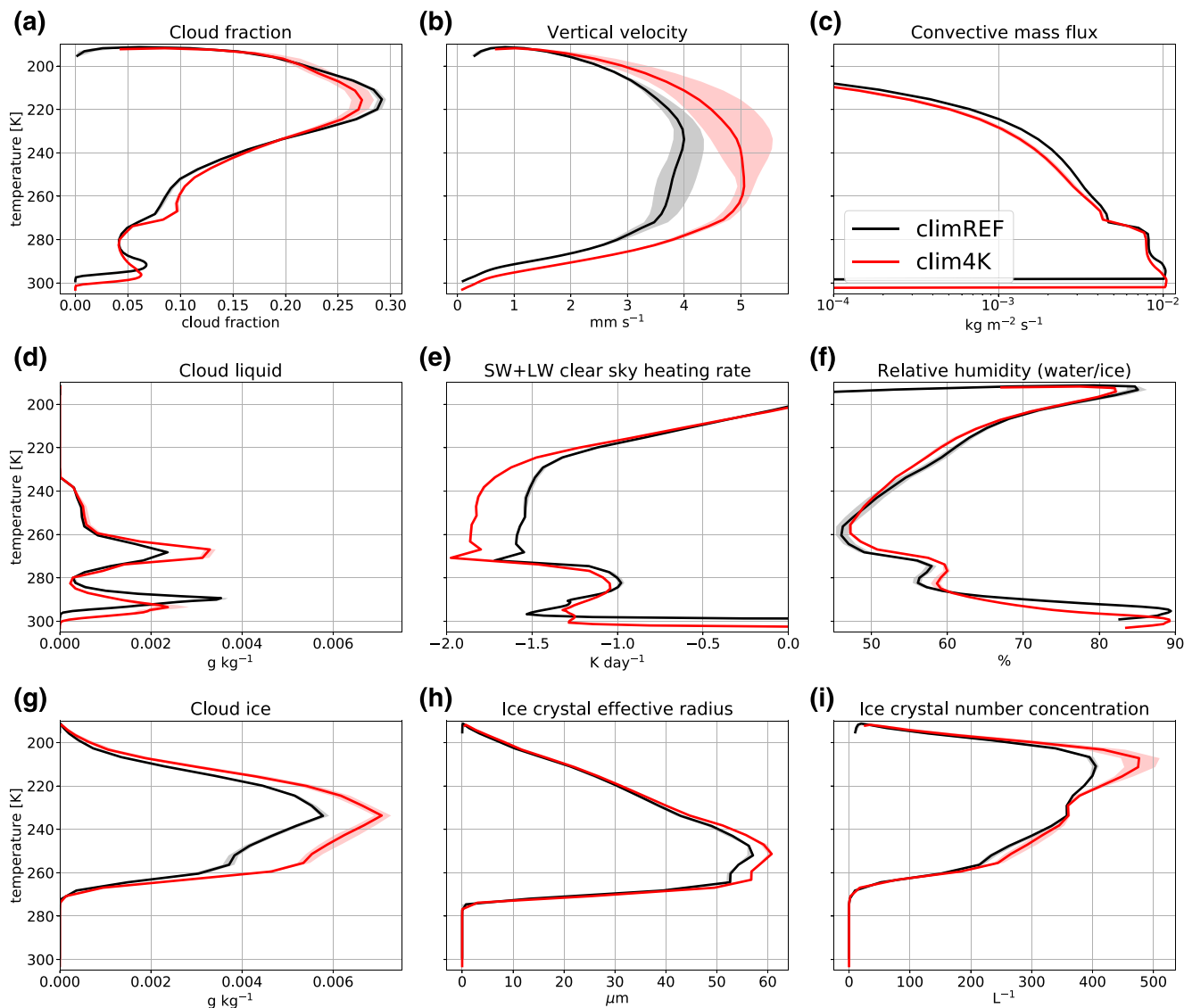


Figure 11. Domain-averaged cloud fraction (a), vertical velocity (b), convective mass flux from the convective parameterization (c), cloud liquid (d), clear sky heating rates (e), the relative humidity with respect to water (for $T > 273\text{K}$), ice (for $T < 253\text{K}$), or a mixture between the two (for $273\text{K} > T > 253\text{K}$) (f), cloud ice (g), in-cloud ice crystal effective radius (h), and in-cloud ice crystal number concentration (i). The quantities are plotted in function of temperature between the surface and approximately the tropopause level. Shaded areas cover the space between all three annually averaged values for each of the simulations.

to the convective mass flux, the resolved mean vertical velocity increases in the global warming simulation (Figure 11b). This is due to an increase in fully convective grid boxes (intense storms with resolved circulation features), as suggested by the increase in relative importance of large scale precipitation (not shown). The upper tropospheric ice crystal effective radius does not change with warming (Figure 11h), while the ice crystal number concentration significantly increases in the uppermost troposphere (Figure 11i).

The domain-mean COD, dominated particularly by changes in high clouds, increases by 8% in the clim4K simulation. The changes in ice clouds lead to a small and negative net CRE change of about 2 W m^{-2} . The cloud feedback decomposition using Zelinka et al. (2016) method shows a strong positive feedback attributed to the increase in cloud altitude (Figure 12a). However, the aforementioned increases in COD lead to a negative feedback that counteracts about half of the altitude feedback.

Figure 12b shows the decomposition of cloud feedback for high clouds ($< 440 \text{ hPa}$) only. The net feedback is near zero, despite large SW and LW components. In the case of high clouds, the positive altitude feedback

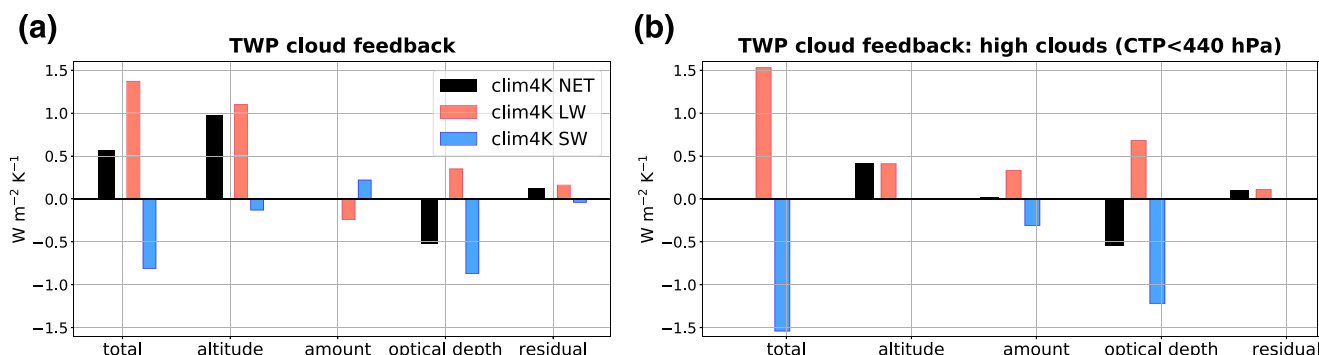


Figure 12. (a) Total net cloud feedback decomposition for the Tropical Western Pacific (TWP) using the Zelinka et al. (2012a) method. (b) Same but for high clouds only (defined as all clouds with a cloud top pressure (CTP) < 440 hPa), showing also the LW (red) and SW (blue) cloud feedback components, using a modified version of Zelinka et al. (2016) method. 440 hPa corresponds to an altitude of about 6.7 km and temperature of about 260K in the TWP.

is fully counteracted by the negative optical depth feedback. The cloud amount feedback has significant SW and LW components that are nearly equal in size. The increased COD does not lead only to a strong SW feedback, but also to a significant positive LW feedback. This is expected due to near neutral net CRE of anvil clouds where an increase in COD would also lead to a significant increase in LWC (Berry & Mace, 2014; Hartmann & Berry, 2017 and also Figure 10). Additional discussion on the computed cloud feedbacks and the associated changes in ISCCP cloud histograms, on which the cloud feedback calculation is based, is given in Text S2.

4.2. Mesoscale Convective System Responses

The cold cloud shield representing very thick and moderately thick high clouds increases from 8.5% (REF) to 9.4% (4K) which is expected from the increase in vertical velocity, domain average cloud ice (Figures 11b and 11d) and the negative high cloud optical depth feedback (Figure 12b). This should be distinguished from the small decrease in total model-simulated high cloud fraction (Figure 11a) as the decrease in very frequent thin high clouds dominates over the increase in thicker high cloud shields. If MCS are tracked by using fixed BT thresholds of 210K and 240K, the number of MCS increases by 60% in the 4K simulation in spite of no change in their lifetime (Table 2). The simulated increase in MCS number is consistent with studies of MCS responses to global warming over the continental United States (Diffenbaugh & Giorgi, 2012; Prein et al., 2017). On the other hand, a percentile-based MCS selection criteria approach does not indicate a much higher MCS number in the 4K simulation. The maximum MCS extent and lifetime remain approximately the same between REF and 4K simulations with both MCS selection methods. The tracked MCS show increases in precipitation, which is expected given the increase in precipitable water under global warming (not shown). Moreover, a warmer climate increases the saturation deficit of the tropical atmosphere, leading to a larger buoyancy of deep convection and consequently an increase in convective available potential energy (CAPE, Seeley & Romps, 2015). The BT-based detection limits do not allow for a good estimate of changes to the evolution and thinning of anvil clouds. In order to study such changes, we return to an analysis along trajectories.

4.3. Cloud and Radiative Responses to Warming Along Detrained Trajectories

4.3.1. Responses of Anvil Cloud Lifetime and Cloud Properties

The QI increases with warming along the trajectories, particularly in the initial thick anvil stage (Figure 8a). The ice crystal number concentration also increases, while the ice crystal effective radius remains initially roughly unchanged and decreases slightly with respect to REF only in the late stage of the anvil evolution (Figure 8c). The lifetime of the anvil cloud remains roughly constant (Figure 7). However, the larger initial QI leads to a 1 h increase in the lifetime of the thick part of the anvil cloud, or a 35% relative increase in the

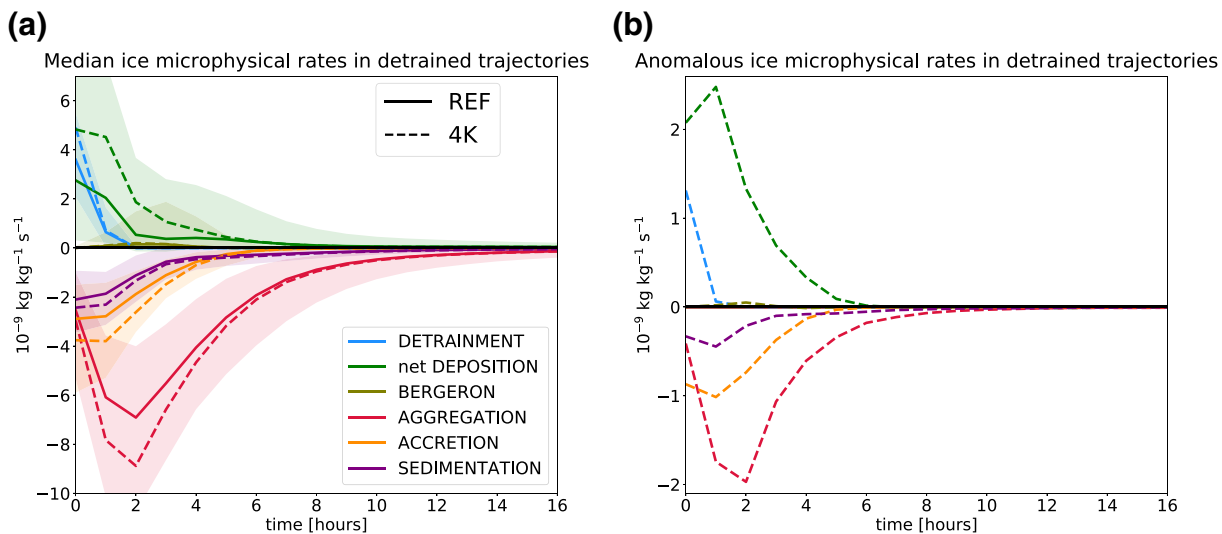


Figure 13. (a) Median sources and sinks of ice in the two simulations. Shaded area represents the spread between the 25th and 75th percentile values for REF. (b) Anomalies of median values of source and sinks of ice with respect to REF.

thick anvil cloud lifetime. The result does not change if we include in the analysis also trajectories influenced by new occurrence of convection in later stages of their evolution (Figure S1).

The microphysical process rate evolution shows a different behavior between the early and late stage of anvil evolution (Figure 13):

- in the early stage of anvil evolution (hour 0–6) both sources and sinks of ice increase in amplitude with respect to REF
- in the late stage of anvil evolution (from hour 7 onward) sources and sinks of ice are similar with respect to REF

The trajectories indicate that the 4K simulation starts at larger QI values, which is a result of tendencies before the start of the trajectory calculation, most likely due to increases in detrainment of ice and vapor by the deep convective scheme. This finding is reinforced by a 40% increase in detrainment of ice and a 80%–100% increase in the net deposition flux (Figure 13) in the initial two trajectory time steps, that are representative of regions of active convection. A large part of the changes in microphysical process rates is in the early anvil stage attributed to the 20% higher initial value of ice mixing ratio. In addition, specific humidity near the deep convective detrainment level increases as the anvil cloud peak shifts to higher altitudes at lower air densities, while remaining at the roughly constant temperature (not shown). This decrease of the average detrainment level pressure from about 235 to about 200 hPa leads to a 5%–10% increase in the deposition flux based on a temperature and pressure dependent depositional growth equation (Lohmann et al., 2016), which explains part of the deposition tendency increase. Moreover, a larger static stability near detrainment level in a warmer world may decrease the mixing of detrained air parcels with environmental air, therefore additionally increasing the QI in the early stage of anvil cloud development.

The rate of loss of atmospheric ice increases proportionally with the increase in QI to first order, which results in only a small increase in thick anvil cloud lifetime in a warmer world (Figure 7). Ice crystal aggregation transfers the larger crystals to snow when they cross a temperature dependent ice crystal effective radius threshold, which spans between 100 and 125 μm for the relevant range of temperatures. Since the trajectories invariably originate near convective events, the initial ice crystal radii are close to the prescribed ice crystal effective radius detrained from the convective parameterization which is set to a constant value of 12 μm , leaving little opportunity for early changes by aggregation between the control and warming runs. The aggregation rate increases by about 20%–30% between hours 1–5 of the anvil development, probably due to a general increase in QI. This is also the likely cause of an increase in both accretion and sedimentation tendencies. In the late stage of anvil evolution, the net deposition slightly decreases compared to REF. This may be connected with a 10% decrease in ice crystal effective radius (Figure 8) leading to a 20%

decrease in surface area available for deposition, given no simulated change in relative humidity and comparable QI between REF and the warming simulation (Figure 11f).

4.3.2. Radiative Responses and Climatic Implications

The increase in QI and ice crystal number with warming leads to a larger SWCRE as shown in Figure 10a. At the same time clouds become more opaque to LW radiation, resulting in an increased LWCRE. The average net CRE for the whole lifecycle of tracked anvil clouds is slightly more negative (Table 3), partially due to increases in COD, consistent with the domain average increases in COD (see Section 4.1). In addition, net CRE is more negative also due to an increase in mean anvil cloud insolation between hour 3 and 11 of cloud development. This is caused by a small shift in the diurnal cycle of MCS (Figure 10b) that peaks at a later hour in the 4K simulation (Figure 5). The insolation-driven changes in SWCRE are partially compensated by the insolation anomalies of the opposite sign at the late stage of the anvil cloud development (after hour 13). However, at that point in the lifecycle, the anvil clouds are not as reflective as in their initial stage, leading only to a minor modulation of the incoming SW radiative flux. In summary, the increases in SWCRE dominate over increases in LWCRE and lead to a more negative net CRE balance over the course of the anvil cloud lifecycle (Table 3 and Figure 10a). This negative CRE anomaly is consistent with the domain-averaged negative high cloud optical depth feedback (Figure 12) and an increased insolation due to a small shift in the MCS diurnal cycle (Figures 10b and 5b).

5. Discussion

5.1. Changes in Upper Tropospheric Ice Properties

5.1.1. Ice Mixing Ratio Increase

The deep convective detrainment, represented by the G. J. Zhang and McFarlane (1995) convective scheme, is proportional to the cloud water and convective mass flux at the base of the cloud. The cloud base convective mass flux is in turn proportional to the rate of consumption of convective available potential energy (CAPE), which is expected to increase in a warmer climate (Seeley & Romps, 2015; Singh et al., 2017). The cloud liquid increases in a warmer climate due to the increased saturation specific humidity. Both of these factors will, due to the approximately constant temperature at the level of deep convective detrainment, lead to a larger upper tropospheric ice mixing ratio due to increases of both detrainment of water vapor and ice. Moreover, the deep convective scheme assumes proportionality between the cloud condensate and the condensate removed by precipitation, leading to an additional reason for the increase of the detrained condensate with warming. Other deep convective parameterizations often use a fixed condensed water threshold, which determines the amount of condensate that is removed by precipitation. Such scheme may respond differently to global warming, possibly leading to no enhancement in detrainment. However, despite the importance of the formulation of convective precipitation formation for climate sensitivity (M. Zhao, 2014; M. Zhao et al., 2016), it is currently not possible to determine which of the two descriptions of precipitation production is more realistic.

Moreover, a recent study by Hartmann et al. (2020) provides a fundamental physical argument in favor of the simulated increase of cloud ice. In a warmer climate, the troposphere expands and lifts the main emission level to lower pressure levels. Assuming a constant temperature and relative humidity at the emission level, the water vapor cooling rate increases with decreasing pressure levels, leading to a more top heavy radiative cooling profile, similarly to what is simulated by the E3SM model (Figure 11e). As the climate in the tracking region can be to a large degree approximated by radiative convective equilibrium, the additional radiative cooling must be compensated by increases in latent heating (Jakob et al., 2019). The increase in cloud ice provides this additional heat (Figure 11g).

5.1.2. Changes in Ice Crystal Effective Radius and Ice Crystal Number Concentration

The upper tropospheric ice crystal effective radius was previously found to be decreasing with decreasing temperature and increasing altitude (Hong & Liu, 2015; Kahn et al., 2018; Krämer et al., 2020), which was associated with the strong temperature dependence of the vapor deposition that limits ice crystal growth (van Diedenhoven et al., 2020). The model is able to reproduce this behavior (Figure 11h), together with the

observed decrease in ice crystal effective radius with increasing temperatures at temperatures warmer than 250K (van Diedenhoven et al., 2020). Note that the warmer end of the considered temperatures is dominated by snow, which is not included in our analysis.

The simulated upper tropospheric ice crystal effective radii do not change significantly in a warmer climate (Figures 11h and 8c), which is probably due to the near constant temperature of deep convective detrainment level (Hartmann & Larson, 2002). Moreover, the possible change of radii with warming is limited by the model assumption of a constant ice crystal effective radius size of 12 μm at detrainment, due to the very simple, 1-moment convective microphysics. This is in contrast with the observed change in cloud top ice crystal effective radius between 2002 and 2016 by the Atmospheric Infrared Sounder observations (Kahn et al., 2018) and a recent GCM modeling study (Zhu & Poulsen, 2019), both showing an increase in ice crystal size.

Given the increase in ice mass detrained by deep convection but an assumed constant detrainment particle size, the model is bound to simulate a higher number of detrained ice crystals, which is a possible reason for the observed ice crystal number concentration increase both in domain average (Figure 11i) and along the tracked trajectories (Figure 8d). The basic thermodynamics of climate change can, however, lead both to an increases in CAPE and updraft velocities in tropical MCS (e.g. Seeley & Romps, 2015; Singh et al., 2017) and an increase in upper tropospheric static stability (Bony et al., 2016; Zelinka & Hartmann, 2010). The stronger deep convective updrafts can at the same time lead to a larger number of smaller newly nucleated ice crystals and provide additional support to carry larger ice crystals toward the cloud top. The increase in static stability implies a decrease in turbulence and the associated updrafts, possibly leading to a smaller number of in-situ nucleated ice crystals that can grow to larger size. It is currently not clear which of the proposed effects may dominate the changes in microphysical properties of anvil clouds and what could be the climatic role of such changes.

5.2. Implications for Tropical High Cloud Feedbacks

Figure 14 summarizes the main findings of the previous section. The QI in thick anvils increases due to increased detrainment tendency from deep convective cores and increased deposition flux. The increase in vapor deposition may also be connected to increased detrainment as the detraining air is assumed to be saturated. This leads to an increased COD and a negative net CRE anomaly in the early stage of the anvil lifecycle. The changes are smaller in aged thin anvil clouds, as the sinks of ice, particularly snow formation, becomes more efficient in removing the excess QI. At this point we take a step further to transform the net CRE values of Table 3 into climate feedbacks by dividing the change in net CRE along trajectories by the increase in globally averaged surface temperatures and adding a derived cloud masking correction term, as explained in Appendix A. The computed climate feedback along detrained trajectories is small and positive for the 4K simulation and consistent with the results of the 3 years long clim4K simulation (Figure 12a) as well as with the literature finding a robust positive tropical cloud feedback (Boucher et al., 2013; Zelinka et al., 2012b, 2013; Zelinka & Hartmann, 2010) with the dominant cloud altitude LW feedback component due to a 1–1.5 km increase in high cloud altitude.

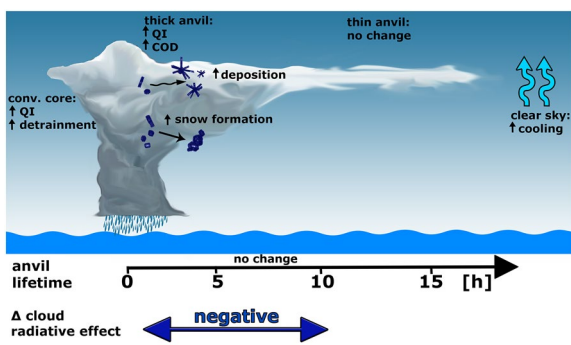


Figure 14. Summary sketch highlighting major changes with global warming. The increase in cloud altitude is omitted from the sketch.

Our simulations reveal in addition an increase in perceptible water and large-scale updraft velocities with global warming that lead to increasing condensed water content at temperatures below freezing, despite a counteracting decrease in the convective mass flux. The anvil cloud peak stays at approximately the same temperature level consistent with the FAT theory (Hartmann & Larson, 2002). When clouds shift in altitude, they shift to an environment with higher static stability, which according to Bony et al. (2016) implies a decreased convective detrainment and a decrease in anvil cloud fraction. In our simulations anvil cloud fraction decreases, but domain-averaged cloud ice content increases, leading to a larger optical depth of remaining anvil clouds and a negative optical depth feedback.

We also observed increases in ice removal rates with warming (Figure 13) due to an increase in anvil cloud precipitation efficiency by ice crystal aggregation and accretion of ice crystals by snow. However, most of this increase in precipitation (snow) formation is due to a higher QI at the starting points of anvil trajectories near the main detrainment level. Moreover, it is not only the sinks but also the sources of ice that increase, in particular the net deposition flux, leading to no change in anvil cloud lifetime nor any substantial shifts of the proportion of thick versus thin anvil clouds (Figure 7). The simulated changes in anvil clouds are therefore different from the microphysical Iris hypothesis and its negative anvil cloud feedback proposed by Lindzen et al. (2001).

5.3. Potential Changes of Anvil Cloud Diurnal Cycle and the Associated Radiative Impacts

The average local time of peak cold cloud shield area of tracked MCS shifts from about midnight in REF simulation to 4 a.m. in the 4K simulation, because more MCS peak in the morning hours (Figure 5). This increases the SWCRE and leads to an additional negative (diurnal) cloud feedback component that cannot be evaluated with the cloud feedback decomposition method used here, because the ISCCP simulator, which it is based on, represents daytime average cloud fraction computed from 3-hourly instantaneous snapshots in sunlit gridboxes, meaning that it is in current form not suitable for studying variations in the diurnal cycle of clouds. We additionally compute CRE by assuming diurnally averaged insolation of 390 W m^{-2} , representative of the domain mean insolation during the months June–August in the tracking region, which increases the net CRE budget by 2.4 W m^{-2} , implying a $0.5 \text{ W m}^{-2} \text{ K}^{-1}$ larger net cloud feedback (Table 3). In other words, the more negative SWCRE balance when using model calculated insolation instead of its diurnal average leads to a negative diurnal cycle component of cloud feedback of $0.5 \text{ W m}^{-2} \text{ K}^{-1}$, confirming the role of changes in insolation presented in Section 4.3.2. The magnitude of the diurnal cycle component of the cloud feedback is comparable to the net cloud feedback for the TWP region, so feedbacks associated with the diurnal cycle could be substantial and are worth investigating in future studies.

5.4. Study Limitations

The goal of this study is to provide a better understanding of the anvil cloud evolution in present and future warmer climate by using an intuitive, ice crystal following Lagrangian perspective. Models are currently the only possible way to provide such insights into cloud lifecycles due to limitations in in-situ and satellite observational data. While the method applied indeed provides valuable insights into the behavior of the model, the reader should be aware of its possible limitations as outlined below.

5.4.1. Statistical Robustness and Study Region

The core part of the study (MCS tracking and trajectory analysis) relies on a 3-month simulation following a 8 day spin up period. 92 simulated days are enough to represent part of the tropical intraseasonal variability at the synoptic timescale with disturbances of sizes of about 1,000 km and timescales of 1–10 days encompassing typical convectively coupled equatorial waves (Kiladis et al., 2009). The length of the simulation is not long enough to encompass a whole possible cycle of the Madden-Julian oscillation with a typical period of 30–70 days. We note that the spin up period is too short to allow a complete adjustment of the tropical overturning circulation, which has a timescale of about 1 month.

However, while this may influence the number of tracked MCS, it is not expected to have a large impact on the anvil cloud lifecycle itself. The anvil decay is primarily driven by processes that operate on a fast timescale like microphysics and radiation, and we have sampled many occurrences of the anvil decay process. Interannual variability, e.g. ENSO, could be an issue, but the simulations use prescribed SST, which prevents the model drift into a different ENSO phase allowing for a better comparison between the simulations. Nevertheless, the simulations used for computing mean climatic values in the region of interest in Section 4.1 are run for only 3 years, which is not enough for computing reliable climatologies. The short simulations therefore introduce uncertainties in CRE and cloud feedback calculations, and suggest an interannual variability in mean June–August net CRE of about 0.5 W m^{-2} in the tracking region, computed from the 3 years of available model output, which is smaller than the magnitude of the net CRE anomalies listed in Table 3.

The qualitative features of the analysis are therefore probably quite robust, while the uncertainty in the quantitative amplitude may be considerable.

Our study focuses on changes in only one of the tropical regions of frequent deep convection. However, as shown by Figure S4, changes in the tracking region (Figure 11) are in all plotted quantities but one (vertical velocity) consistent with the zonally averaged responses, giving more weight to our results.

5.4.2. Trajectory Calculation

We use an offline method for calculating trajectories from model resolved large-scale motions. The E3SM model time step is set to 15 min while the output time step is archived at 1 h intervals because of storage space limitations. E3SM therefore evolves on timescales that are shorter than resolved from the archived data (4 updates of velocity and microphysical fields are performed online within the archival time interval), which introduces minor biases in trajectory calculations. A study by Miltenberger et al. (2013) based on a regional weather prediction model shows only minor horizontal and vertical biases in the offline trajectory calculation when comparing offline calculated trajectories using 1-hourly model output with the online calculated trajectories for the model resolution of 14 km with the model time step of 40 s.

5.4.3. Simulated Interaction of Convective and Large-Scale Cloud Processes

A large part of the presented results strongly depends on the way E3SM simulates deep convection with the help of a modified version of the G. J. Zhang and McFarlane (1995) convective scheme, described in Xie et al. (2018). The scheme is meant to reduce CAPE over the course of a timescale that can be tuned. The model was found to underestimate BT of the strongest convective events, and at the same time overestimate the frequency of intermediate BT. These biases indicate a too shallow convective cloud top layer and/or a too small convective mass flux above about 10 km altitude which is consistent with findings by Xie et al. (2018) and Y. Zhang et al. (2019). This may be caused by a too large convective entrainment (Wang & Zhang, 2018) and/or a low mid tropospheric humidity bias (Xie et al., 2018). Moreover, convection is typically found to be shallower in models with higher vertical resolution (like E3SM) compared to those with coarser resolution (e.g. CESM) as a higher vertical resolution can lead to stronger vertical gradients in humidity, heating, and static stability (Rasch et al., 2019).

The deep convective scheme uses a simple thermodynamical treatment of clouds, with a temperature dependent partitioning of detrained condensate between liquid and ice. Besides condensate it also detrains vapor, leading to a moistening of the upper troposphere. The convective microphysics is very simplified and only 1-moment in contrast to the 2-moment stratiform cloud microphysical scheme. The convective part of the code therefore does not explicitly calculate ice crystal radii, while the 2-moment stratiform cloud microphysics requires a mass and size or number of detrained ice particles. The convective scheme provides this information in an arbitrary way, the detrained ice crystal effective radius is a tunable parameter, set to 12 μm in the model version used here. This is inconsistent with observational evidence, which shows that the ice particle size in convective cores decreases with altitude (Van Diedenhoven et al., 2016, 2020) and may therefore lead to an underestimation of the lifetime of the detrained ice crystals at the convective cloud tops and overestimation at lower levels. Nevertheless, despite the use of parametrized convection and its associated problems, we found E3SM to reproduce the observed albedo-OLR histogram in the tracking region remarkably well and to simulate MCS in a reliable way compared to geostationary observations of tropical maritime convection.

6. Conclusions

Tropical net CRE is determined by anvil clouds at various stages of evolution. In this study we first used a cold cloud tracking algorithm to follow the evolution of MCS in the Tropical Western Pacific. The MCS simulated by E3SM were compared with the observed MCS from 3 months of Himawari geostationary

satellite data. The comparison showed that the model is, despite some deficiencies, able to reproduce many features of the observed albedo-OLR pairings representing anvil cloud decay as well as MCS and their diurnal cycle. We find that cloud ice amount increases on a warmer Earth, which leads to a negative cloud optical depth feedback. However, the net cloud feedback is positive due to the dominant positive cloud altitude feedback.

In a second analysis step, we diagnosed anvil properties following trajectories launched from gridboxes with active convection at the peak of the MCS lifecycle in the E3SM simulations. These trajectories follow air parcels from the top of deep convective clouds throughout the evolution of the anvil clouds, from their initial thick to final thin stage. We use the trajectories to estimate the anvil cloud lifetime, which was found to be about 15 h. The anvil properties and their CRE initially evolve very quickly, with the thick anvil stage lasting only about 2–4 h, despite a supporting dynamical forcing in the form of the strong updraft velocity. The anvil gradually continues to decay with decreasing QI and ice crystal number concentration, resulting in decreases of both SWCRE and LWCRC. The dominant source of ice mass is ice crystal growth by deposition, while the dominant sinks are snow formation by ice crystal aggregation (ice is converted to snow when crossing the aggregation cutoff size) and in the first 5 h of evolution also accretion (ice is removed when scavenged by falling snow). Sedimentation of ice crystals plays only a secondary role.

We evaluated changing anvil cloud properties using present day SSTs, and SSTs incremented by a uniform 4K increase to identify changes that might occur in anvils with global warming. Figure 14 represents a summary of the main simulated changes in clouds. In general, we observe an increase in COD for thick high clouds due to an increase in detrained QI and vapor. Ice mass sources and sinks increase, leaving the anvil cloud lifetime roughly unchanged. Changes to anvil microphysics lead to more negative SWCRE in the thick and intermediately thick anvil cloud stage in the first 10 h of anvil cloud evolution. The changes in the thin anvil stage are small, which leads to a net negative CRE response along the full anvil lifecycle.

The estimation of cloud feedbacks along trajectories indicated a feedback of about $0.5 \text{ W m}^{-2} \text{ K}^{-1}$. This result is consistent with the mean climate feedback computed with the help of radiative kernels in which the positive altitude feedback dominates over a smaller contribution due to the COD increase. The feedback may also have a negative component due to a shift in peak deep convective activity occurring at a later time in the morning, leading to more reflected SW radiation.

Our study shows how a Lagrangian approach can provide an in-depth and more intuitive perspective on anvil cloud evolution and its changes with global warming. Our approach is complementary to the standard global or regionally averaged climate feedback decompositions. In particular, it offers the following advantages over the standard mean climate perspective:

- It gives a direct estimation of cloud lifetimes
- It offers an intuitive perspective on microphysical processes that control anvil evolution and radiative properties. It also allows computing Lagrangian mass budgets
- It provides a straightforward and unbiased way of separating cloud responses based on cloud development stage

Such Lagrangian approaches are needed if we want to fully understand the mechanisms of the anvil cloud lifecycle and how they respond to global warming. A Lagrangian, air parcel or hydrometer following approach can provide new insights into the evolution of cloud and other climate processes. The use of Lagrangian methods in high resolution models is still limited and should be made a priority, particularly by the implementation of online trajectory modules (Miltenberger et al., 2013). Follow-up studies using Lagrangian methods could consider extending their simulations from months to years to better control noise due to natural variability. An increased statistical significance of the tracked features would for example open up new opportunities for studying potential radiative feedbacks caused by changes in the diurnal cycle of clouds, which currently cannot be captured by cloud feedback decomposition methods.

Appendix A: Cloud Feedback Estimation from Changes in net CRE Along Detrained Trajectories

CRE are defined as a difference between all-sky and clear sky radiative fluxes. A change in CRE between the reference and a warmer climate is not equivalent to the change in cloud feedbacks, although the patterns of change generally resemble each other (e.g. Figure 11 in Soden et al., 2008). While cloud feedbacks refer only to the radiative effects of changes in cloud properties with warming, CRE are defined as a difference between full and clear sky radiative fluxes and therefore depends both on changes in clouds and their radiative properties as well as changes in clear sky radiation. In simulations with increased SSTs the atmospheric opacity increases mainly due to increased water vapor concentrations. This effect is stronger in clear sky regions and thus leads to a more negative CRE response compared with cloud feedbacks (Ceppi et al., 2017).

An accurate way of estimating cloud masking adjustments is to use technically challenging partial radiative perturbation methods (Colman, 2003; Soden et al., 2004), which goes beyond the scope of our work. We therefore estimate a cloud masking correction term by using the difference between the computed CRE values for months June–August in the 3-years long simulation (row one in Table A1), normalized by the change in global surface temperature in the respective simulation (row two in Table A1), and the cloud feedback calculations with the help of radiative kernels (Zelinka et al., 2012a) (row four in Table A1). The derived cloud masking agrees well with the masking terms computed from offline radiative calculations with a series of GCMs (Soden et al., 2008; Yoshimori et al., 2020; Zelinka et al., 2013).

Table A1

3 years JJA Average Net Cloud Radiative Effects (CRE) Anomalies With Respect To Reference Simulation, Net Cloud Feedback Calculated By Using Zelinka et al. (2012a) Radiative Kernels for Tropical Western Pacific. The Adjustment Term is Computed as a Difference Between the Cloud Feedback and Normalized CRE Value.

	clim4K
Δ NET CRE (W m^{-2})	−2.03
Δ temperature (K)	4.31
$\frac{\Delta \text{NET CRE}}{\Delta \text{temperature}}$ ($\text{W m}^{-2} \text{K}^{-1}$)	−0.47
calculated feedback ($\text{W m}^{-2} \text{K}^{-1}$)	0.52
estimated CRE adjustment ($\text{W m}^{-2} \text{K}^{-1}$)	0.99

Appendix B: Calculation of Ice Crystal Effective Radius

The ice size distribution is represented by a gamma function as

$$\Phi(D) = N_0 D \exp^{-\lambda D} \quad (\text{B1})$$

where D is the diameter, N_0 the intercept parameter, and λ is the slope parameter that is defined as:

$$\lambda = \left[\frac{\pi \rho N}{q} \right]^{\frac{1}{3}} \quad (\text{B2})$$

where ρ is the assumed bulk ice density of 500 kg m^{-3} , q is the ice mass mixing ratio, and N is the ice number concentration.

The effective radius is defined as the ratio of the third and second moments of the ice distribution, which can be expressed as

$$r_e = \frac{3\rho}{2\lambda\rho_i} \quad (\text{B3})$$

ρ_i is the bulk density of pure ice (917 kg m⁻³). More details on the assumed ice distribution can be found in Morrison and Gettelman (2008) and Neale et al. (2012).

The description above refers to the effective radius that was used in this publication. In contrast, the E3SM radiation code additionally uses an assumption of ice crystal shape in calculations of mass-weighted extinction and single scattering albedo Neale et al. (2012). The assumption considers quasispherical ice crystals for shortwave wavelengths (Mitchell et al., 1996; Nousiainen & McFarquhar, 2004) and a mixture composed of 50% quasispherical, 30% irregular, and 20% bullet rosettes ice particles for the longwave part of the spectrum, based on the observations of midlatitude cirrus for the small ice mode (Lawson et al., 2006). Snow is also radiatively active in E3SM, with an assumed particle habit composed of 50% bullet rosettes, 43% irregular ice, and 7% hexagonal columns, based on the observations for the large ice mode at -45 °C by Lawson et al. (2006).

Data Availability Statement

Simulations were performed using computer resources provided by EMSL (grid.436,923.9), a DOE Office of Science User Facility sponsored by the Office of Biological and Environmental Research and located at Pacific Northwest National Laboratory. The Himawari-8 data were obtained from the Atmospheric Science Data Center of the NASA Langley Research Center and are available at <https://earthdata.nasa.gov/>. The satellite data from the A-Train Integrated CALIPSO, CloudSat, CERES, and MODIS Merged Product Release B1 (CCCM) were obtained from <https://search.earthdata.nasa.gov>. The data and plotting scripts will be made available on Zenodo (10.5281/zenodo.3893226) after the final acceptance of the publication.

Acknowledgments

The authors thank Michael Sprenger for the help with the implementation of Lagranto into E3SM model. The authors thank Peter Blossey for numerous valuable comments that helped improve our methods and the manuscript. Thanks to Mark Zelinka for sharing the cloud radiative kernels and the cloud feedback decomposition script. Thanks to Adam Sokol for the help in the estimation of the relation between cloud optical depth and brightness temperature. This research was partially supported as part of the Energy Exascale Earth System Model (E3SM) project, funded by the U.S. Department of Energy, Office of Science, Office of Biological and Environmental Research. BG acknowledges support by the Swiss National Science Foundation projects P2EZP2_178485 and P400P2191112 and by the National Science Foundation under Grant AGS-1549579. C. J. Wall is supported by the NOAA Climate and Global Change Postdoctoral Fellowship Program, administered by UCAR's Cooperative Programs for the Advancement of Earth System Science (CPAESS) under award #NA18NWS4620043. B. M. Dütsch acknowledges support by the Swiss National Science Foundation project P2EZP2_178439.

References

Avery, M., Winker, D., Heymsfield, A., Vaughan, M., Young, S., Hu, Y., et al. (2012). Cloud ice water content retrieved from the CALIOP space-based LIDAR. *Geophysical Research Letters*, 39(5), 2–7. <https://doi.org/10.1029/2011GL050545>

Berry, E., & Mace, G. G. (2014). Cloud properties and radiative effects of the Asian summer monsoon derived from A-Train data. *Journal of Geophysical Research: Atmospheres*, 119, 9492–9508. <https://doi.org/10.1002/2014JD021458>

Bessho, K., Date, K., Hayashi, M., Ikeda, A., Imai, T., Inoue, H., et al. (2016). An introduction to Himawari-8/9- Japan's new-generation geostationary meteorological satellites. *Journal of the Meteorological Society of Japan*, 94(2), 151–183. <https://doi.org/10.2151/jmsj.2016-009>

Bodas-Salcedo, A., Webb, M. J., Bony, S., Chepfer, H., Dufresne, J. L., Klein, S. A., et al. (2011). COSP: Satellite simulation software for model assessment. *Bulletin of the American Meteorological Society*, 92(8), 1023–1043. <https://doi.org/10.1175/2011BAMS2856.1>

Bony, S., Stevens, B., Coppin, D., Becker, T., Reed, K. A., Voigt, A., et al. (2016). Thermodynamic control of anvil cloud amount. *Proceedings of the National Academy of Sciences*, 113(32), 8927–8932. <https://doi.org/10.1073/pnas.1601472113>

Boucher, O., Randall, D., Artaxo, P., Christopher, B., Feingold, G., Forster, P., et al. (2013). Clouds and aerosols. In T. F. Stocker, D. Qin, G.-K. Plattner, & M. Tignor (Eds.), *Climate change 2013: The physical science basis. Contribution of working group I to the fifth assessment report of the intergovernmental panel on climate change*, 7, (pp.571–632) Cambridge, UK and New York, NY, USA: Cambridge University Press. Retrieved from https://www.ipcc.ch/site/assets/uploads/2018/02/WG1AR5_Chapter07_FINAL-1.pdf

Bouniol, D., Roca, R., Fiolleau, T., & Poan, D. E. (2016). Macrophysical, microphysical and radiative properties of tropical mesoscale convective systems over their life cycle. *Journal of Climate*, 29(9), 3353–3371. <https://doi.org/10.1175/JCLI-D-15-0551.1>

Caldwell, P. M., Mametjanov, A., Tang, Q., Van Roekel, L. P., Golaz, J. C., Lin, W., et al. (2019). The DOE E3SM coupled model version 1: Description and results at high resolution. *Journal of Advances in Modeling Earth Systems*, 11(12), 4095–4146. <https://doi.org/10.1029/2019MS001870>

Ceppi, P., Brient, F., Zelinka, M. D., & Hartmann, D. L. (2017). Cloud feedback mechanisms and their representation in global climate models. *Wiley Interdisciplinary Reviews on Climate Change*, 8, e465. <https://doi.org/10.1002/wcc.465>

Choi, Y.-S., Kim, W., Yeh, S.-W., Masunaga, H., Kwon, M.-J., Jo, H.-S., et al. (2017). Revisiting the iris effect of tropical cirrus clouds with TRMM and A-Train satellite data. *Journal of Geophysical Research: Atmospheres*, 122, 5917–5931. <https://doi.org/10.1002/2016JD025827>

Colman, R. (2003). A comparison of climate feedbacks in general circulation models. *Climate Dynamics*, 20(7–8), 865–873. <https://doi.org/10.1007/s00382-003-0310-z>

Dee, D. P., Uppala, S. M., Simmons, A. J., Berrisford, P., Poli, P., Kobayashi, S., et al. (2011). The ERA-Interim reanalysis: Configuration and performance of the data assimilation system. *Quarterly Journal of the Royal Meteorological Society*, 137(656), 553–597. <https://doi.org/10.1002/qj.828>

Dennis, J. M., Edwards, J., Evans, K. J., Guba, O., Lauritzen, P. H., Mirin, A. A., et al. (2012). CAM-SE: A scalable spectral element dynamical core for the community atmosphere model. *International Journal of High Performance Computing Applications*, 26(1), 74–89. <https://doi.org/10.1177/1094342011428142>

Diffenbaugh, N. S., & Giorgi, F. (2012). Climate change hotspots in the CMIP5 global climate model ensemble. *Climatic Change*, 114(3–4), 813–822. <https://doi.org/10.1007/s10584-012-0570-x>

Fiolleau, T., & Roca, R. (2013). An algorithm for the detection and tracking of tropical mesoscale convective systems using infrared images from geostationary satellite. *IEEE Transactions on Geoscience and Remote Sensing*, 51(7), 4302–4315. <https://doi.org/10.1109/TGRS.2012.2227762>

Fischer, E. M., & Knutti, R. (2015). Anthropogenic contribution to global occurrence of heavy-precipitation and high-temperature extremes. *Nature Climate Change*, 5(6), 560–564. <https://doi.org/10.1038/nclimate2617>

Fischer, E. M., & Knutti, R. (2016). Observed heavy precipitation increase confirms theory and early models. *Nature Climate Change*, 6(11), 986–991. <https://doi.org/10.1038/nclimate3110>

Fu, Q., Baker, M., & Hartmann, D. L. (2002). Tropical cirrus and water vapor: an effective Earth infrared iris feedback? *Atmospheric Chemistry and Physics*, 2, 31–37. <https://doi.org/10.5194/acp-2-31-2002>

Gehlot, S., & Quaas, J. (2012). Convection-climate feedbacks in the ECHAM5 general circulation model: Evaluation of cirrus cloud life cycles with ISCCP satellite data from a Lagrangian trajectory perspective. *Journal of Climate*, 25(15), 5241–5259. <https://doi.org/10.1175/JCLI-D-11-00345.1>

Gettelman, A., Liu, X., Ghan, S. J., Morrison, H., Park, S., Conley, a. J., et al. (2010). Global simulations of ice nucleation and ice supersaturation with an improved cloud scheme in the community atmosphere model. *Journal of Geophysical Research*, 115, 1–19. <https://doi.org/10.1029/2009JD013797>

Gettelman, A., & Morrison, H. (2015). Advanced two-moment bulk microphysics for global models. Part I: Off-line tests and comparison with other schemes. *Journal of Climate*, 28(3), 1268–1287. <https://doi.org/10.1175/JCLI-D-14-00102.1>

Golaz, J., Caldwell, P. M., Van Roekel, L. P., Petersen, M. R., Tang, Q., Wolfe, J. D., et al. (2019). The DOE E3SM coupled model version 1: Overview and evaluation at standard resolution. *Journal of Advances in Modeling Earth Systems*, 11(7), 2089–2129. <https://doi.org/10.1029/2018ms001603>

Golaz, J.-C., Larson, V. E., Cotton, W. R., A PDF-based model for boundary layer clouds. Part I: method and model description (2002). *Journal of the Atmospheric Sciences*, 59(24), 3540–3551. [https://doi.org/10.1175/1520-0469\(2002\)059\(3540:APBMBF\)2.0.CO;2](https://doi.org/10.1175/1520-0469(2002)059(3540:APBMBF)2.0.CO;2)

Harrop, B. E., & Hartmann, D. L. (2012). Testing the role of radiation in determining tropical cloud-top temperature. *Journal of Climate*, 25(17), 5731–5747. <https://doi.org/10.1175/JCLI-D-11-00445.1>

Harrop, B. E., & Hartmann, D. L. (2016). The role of cloud radiative heating within the atmosphere on the high cloud amount and top-of-atmosphere cloud radiative effect. *Journal of Advances in Modeling Earth Systems*, 8, 1391–1410. <https://doi.org/10.1002/2016MS000670>

Hartmann, D. L., & Berry, S. E. (2017). The balanced radiative effect of tropical anvil clouds. *Journal of Geophysical Research: Atmospheres*, 122(9), 5003–5020. <https://doi.org/10.1002/2017JD026460>

Hartmann, D. L., Blossey, P. N., & Dygert, B. D. (2019). Convection and climate: What have we learned from simple models and simplified settings? *Current Climate Change Reports*, 5(3), 196–206. <https://doi.org/10.1007/s40641-019-00136-9>

Hartmann, D. L., Dygert, B. D., Fu, Q., & Blossey, P. N. (2020). The warming physics of tropic world: Part 1 mean state. *Journal of Earth and Space Science. Open Archive*, 1–27. <https://doi.org/10.1002/essoar.10503489.1>

Hartmann, D. L., & Larson, K. (2002). An important constraint on tropical cloud: Climate feedback. *Geophysical Research Letters*, 29(20), 1951. <https://doi.org/10.1029/2002GL015835>

Hartmann, D. L., & Michelsen, M. L. (2002). No evidence for iris. *BAMS*, 83(2), 249–254. [https://doi.org/10.1175/1520-0477\(2002\)083\(0249:NEFI\)2.3.CO;2](https://doi.org/10.1175/1520-0477(2002)083(0249:NEFI)2.3.CO;2)

Hong, Y., & Liu, G. (2015). The characteristics of ice cloud properties derived from CloudSat and CALIPSO measurements. *Journal of Climate*, 28, 3880–3901. <https://doi.org/10.1175/JCLI-D-14-00666.1>

Houze, R. A. J. (2004). Mesoscale convective systems. *Reviews of Geophysics*, 42, 1–43. <https://doi.org/10.1029/2004RG000150.1>

Hurrell, J. W., Hack, J. J., Shea, D., Caron, J. M., & Rosinski, J. (2008). A new sea surface temperature and sea ice boundary dataset for the community atmospheric model. *Journal of Climate*, 21(19), 5145–5153. <https://doi.org/10.1175/2008JCLI2292.1>

Iacono, M. J., Delamere, J. S., Mlawer, E. J., Shephard, M. W., Clough, S. A., & Collins, W. D. (2008). Radiative forcing by long-lived greenhouse gases: Calculations with the AER radiative transfer models. *Journal of Geophysical Research*, 113(13), 2–9. <https://doi.org/10.1029/2008JD009944>

Jakob, C., Singh, M. S., & Jungandreas, L. (2019). Radiative convective equilibrium and organized convection: An observational perspective. *Journal of Geophysical Research: Atmospheres*, 124(10), 5418–5430. <https://doi.org/10.1029/2018JD030092>

Jensen, E. J., van den Heever, S. C., & Grant, L. D. (2018). The lifecycles of ice crystals detrained from the tops of deep convection. *Journal of Geophysical Research: Atmospheres*, 123(17), 1–11. <https://doi.org/10.1029/2018JD028832>

Kahn, B. H., Takahashi, H., Stephens, G. L., Yue, Q., Delanoë, J., Manipon, G., et al. (2018). Ice cloud microphysical trends observed by the atmospheric infrared sounder. *Atmospheric Chemistry and Physics*, 18(14), 10715–10739. <https://doi.org/10.5194/acp-18-10715-2018>

Kato, S., Rose, F. G., Sun-Mack, S., Miller, W. F., Chen, Y., Rutan, D. A., et al. (2011). Improvements of top-of-atmosphere and surface irradiance computations with CALIPSO-, CloudSat-, and MODIS-derived cloud and aerosol properties. *Journal of Geophysical Research*, 116(19), 1–21. <https://doi.org/10.1029/2011JD016050>

Khairoutdinov, M., & Emanuel, K. (2013). Rotating radiative-convective equilibrium simulated by a cloud-resolving model. *Journal of Advances in Modeling Earth Systems*, 5(4), 816–825. <https://doi.org/10.1002/2013ms000253>

Kiladis, G. N., Wheeler, M. C., Haertel, P. T., Straub, K. H., & Roundy, P. E. (2009). Convectively coupled equatorial waves. *Reviews of Geophysics*, 47(RG2003), 1–22. <https://doi.org/10.1029/2008RG000266.1.HISTORICAL>

Klein, S. A., & Jakob, C. (1999). Validation and sensitivities of frontal clouds simulated by the ECMWF model. *Monthly Weather Review*, 127(10), 2514–2531. [https://doi.org/10.1175/1520-0493\(1999\)127\(2514:VASOFC\)2.0.CO;2](https://doi.org/10.1175/1520-0493(1999)127(2514:VASOFC)2.0.CO;2)

Krämer, M., Rolf, C., Spelten, N., Afchine, A., Fahey, D., Jensen, E., et al. (2020). A microphysics guide to Cirrus-part II: Climatologies of clouds and humidity from observations. *Atmospheric Chemistry and Physics*, 20(21), 1–63. <https://doi.org/10.5194/acp-2020-40>

Kuang, Z., & Hartmann, D. L. (2007). Testing the fixed anvil temperature hypothesis in a cloud-resolving model. *Journal of Climate*, 20(10), 2051–2057. <https://doi.org/10.1175/JCLI4124.1>

Kubar, T. L., Hartmann, D. L., & Wood, R. (2007). Radiative and convective driving of tropical high clouds. *Journal of Climate*, 20(22), 5510–5526. <https://doi.org/10.1175/2007JCLI1628.1>

Larson, V. E., & Golaz, J.-C. (2005). Using probability density functions to derive consistent closure relationships among higher-order moments. *Monthly Weather Review*, 133(4), 1023–1042. <https://doi.org/10.1175/MWR2902.1>

Lawson, R. P., Baker, B., Pilson, B., & Mo, Q. (2006). In situ observations of the microphysical properties of wave, cirrus, and anvil clouds-part II: Cirrus clouds. *Journal of the Atmospheric Sciences*, 63(12), 3186–3203. <https://doi.org/10.1175/JAS3803.1>

Lindzen, R. S., & Choi, Y. S. (2011). On the observational determination of climate sensitivity and its implications. *Asia-Pacific Journal of Atmospheric Science*, 47(4), 377–390. <https://doi.org/10.1007/s13143-011-0023-x>

Lindzen, R. S., Chou, M. D., & Hou, A. Y. (2001). Does the earth have an adaptive infrared iris? *Bulletin of the American Meteorological Society*, 82(3), 417–432. [https://doi.org/10.1175/1520-0477\(2001\)082\(0417:DTEHAA\)2.3](https://doi.org/10.1175/1520-0477(2001)082(0417:DTEHAA)2.3)

Lohmann, U., Lüönd, F., & Mahrt, F. (2016). *An introduction to clouds: From the microscale to climate* (pp. 1–25), Cambridge, UK. Cambridge University Press. Retrieved from <https://doi.org/10.1017/CBO9781139087513>

Luo, Z., & Rossow, W. B. (2004). Characterizing tropical cirrus life cycle, evolution, and interaction with upper-tropospheric water vapor using Lagrangian trajectory analysis of satellite observations. *Journal of Climate*, 17, 4541–4563. <https://doi.org/10.1175/3222.1>

Mace, G. G., & Berry, E. (2017). Using active remote sensing to evaluate cloud-climate feedbacks: A review and a look to the future. *Current Climate Change Reports*, 8(3), 185–192. <https://doi.org/10.1007/s40641-017-0067-9>

Mace, G. G., Deng, M., Soden, B., & Zipser, E. (2006). Association of tropical cirrus in the 10–15 km layer with deep convective sources: An observational study combining millimetre radar data and satellite-derived trajectories. *Journal of the Atmospheric Sciences*, 63(2), 480–503. <https://doi.org/10.1175/JAS3627.1>

Machado, L. A., Rossow, W. B., Guedes, R. L., & Walker, A. W. (1998). Life cycle variations of mesoscale convective systems over the Americas. *Monthly Weather Review*, 126(6), 1630–1654. [https://doi.org/10.1175/1520-0493\(1998\)126\(1630:LCVOMC\)2.0.CO;2](https://doi.org/10.1175/1520-0493(1998)126(1630:LCVOMC)2.0.CO;2)

Mapes, B. E., & Houze, R. A. (1993). Cloud clusters and superclusters over the oceanic warm pool. *Monthly Weather Review*, 121(5), 1398–1415. [https://doi.org/10.1175/1520-0493\(1993\)121\(1398:ccasot\)2.0.co;2](https://doi.org/10.1175/1520-0493(1993)121(1398:ccasot)2.0.co;2)

Marvel, K., Zelinka, M., Klein, S. A., Bonfils, C., Caldwell, P., Doutriaux, C., et al. (2015). External influences on modeled and observed cloud trends. *Journal of Climate*, 28(12), 4820–4840. <https://doi.org/10.1175/JCLI-D-14-00734.1>

Mauritsen, T., & Stevens, B. (2015). Missing iris effect as a possible cause of muted hydrological change and high climate sensitivity in models. *Nature Geoscience*, 8(5), 346–351. <https://doi.org/10.1038/ngeo2414>

Meyers, M. P., Demott, P. J., & Cotton, W. R. (1992). New primary ice-nucleation parameterizations in an explicit cloud model. *Journal of Applied Meteorology*, 31(7), 708–721. [https://doi.org/10.1175/1520-0450\(1992\)031\(0708:NPINPI\)2.0.CO;2](https://doi.org/10.1175/1520-0450(1992)031(0708:NPINPI)2.0.CO;2)

Miltenberger, A. K., Pfahl, S., & Wernli, H. (2013). An online trajectory module (version 1.0) for the nonhydrostatic numerical weather prediction model. *COSMO. Geoscience Modeling Device*, 6(6), 1989–2004. <https://doi.org/10.5194/gmd-6-1989-2013>

Mitchell, D. L., Liu, Y., & Macke, A. (1996). Modeling cirrus clouds. Part II: Treatment of radiative properties. *Journal of the Atmospheric Sciences*, 53(20), 2967–2988. [https://doi.org/10.1175/1520-0469\(1996\)053\(2967:MCCPIT\)2.0.CO;2](https://doi.org/10.1175/1520-0469(1996)053(2967:MCCPIT)2.0.CO;2)

Mlawer, E. J., Taubman, J., Brown, P. D., Iacono, M. J., & Clough, S. A. (1997). Radiative transfer for inhomogeneous atmospheres: RRTM, a validated correlatedk model for the longwave. *Journal of Geophysical Research*, 102(D14), 16663–16682. <https://doi.org/10.1029/97JD00237>

Morrison, H., & Gettelman, A. (2008). A new two-moment bulk stratiform cloud microphysics scheme in the community atmosphere model, version 3 (CAM3). Part I: Description and numerical tests. *Journal of Climate*, 21(15), 3642–3659. <https://doi.org/10.1175/2008JCLI2105.1>

Neale, R. B., Gettelman, A., Park, S., Chen, C.-c., Lauritzen, P. H., Williamson, D. L., et al. (2012). *Description of the NCAR community atmosphere model (CAM 5.0). TN-486+STR*, NCAR. https://www.cesm.ucar.edu/models/cesm1.0/cam/docs/description/cam5_desc.pdf

Neale, R. B., Richter, J. H., & Jochum, M. (2008). The impact of convection on ENSO: From a delayed oscillator to a series of events. *Journal of Climate*, 21(22), 5904–5924. <https://doi.org/10.1175/2008JCLI2244>

Nesbitt, S. W., & Zipser, E. J. (2003). The diurnal cycle of rainfall and convective intensity according to three years of TRMM measurements. *Journal of Climate*, 16(10), 1456–1475. <https://doi.org/10.1175/1520-0442-16.10.1456>

Norris, J. R., Allen, R. J., Evan, A. T., Zelinka, M. D., O'Dell, C. W., & Klein, S. A. (2016). Evidence for climate change in the satellite cloud record. *Nature*, 536(7614), 72–75. <https://doi.org/10.1038/NATURE18273>

Nousiainen, T., & McFarquhar, G. M. (2004). Light scattering by quasi-spherical ice crystals. *Journal of the Atmospheric Sciences*, 61(18), 2229–2248. [https://doi.org/10.1175/1520-0469\(2004\)061\(2229:LSBQIC\)2.0.CO;2](https://doi.org/10.1175/1520-0469(2004)061(2229:LSBQIC)2.0.CO;2)

Ohno, T., & Satoh, M. (2018). Roles of cloud microphysics on cloud responses to sea surface temperatures in radiative-convective equilibrium experiments using a high-resolution global nonhydrostatic model. *Journal of Advances in Modeling Earth Systems*, 10, 1970–1989. <https://doi.org/10.1029/2018MS001386>

Ohno, T., Satoh, M., & Noda, A. (2019). Fine vertical resolution radiative convective equilibrium experiments: roles of turbulent mixing on the high cloud response to sea surface temperatures. *Journal of Advances in Modeling Earth Systems*, 11, 1–18. <https://doi.org/10.1029/2019MS001704>

Pendergrass, A. G., & Knutti, R. (2018). The uneven nature of daily precipitation and its change. *Geophysical Research Letters*, 45(21), 11980–11988. <https://doi.org/10.1029/2018GL080298>

Prein, A. F., Liu, C., Ikeda, K., Trier, S. B., Rasmussen, R. M., Holland, G. J., et al. (2017). Increased rainfall volume from future convective storms in the US. *Nature Climate Change*, 7(12), 880–884. <https://doi.org/10.1038/s41558-017-0007-7>

Protopapadaki, S. E., Stuber, C. J., & Feofilov, A. G. (2017). Upper tropospheric cloud systems derived from IR sounders: properties of cirrus anvils in the tropics. *Atmospheric Chemistry and Physics*, 17(6), 3845–3859. <https://doi.org/10.5194/acp-17-3845-2017>

Rasch, P. J., Xie, S., Ma, P.-l., Lin, W., Wang, H., Tang, Q., et al. (2019). An overview of the atmospheric component of the energy exascale earth system model. *Journal of Advances in Modeling Earth Systems*, 11(8), 2377–2411. <https://doi.org/10.1029/2019MS001629>

Rempel, M., Senf, F., & Deneke, H. (2017). Object-based metrics for forecast verification of convective development with geostationary satellite data. *Monthly Weather Review*, 145(8), 3161–3178. <https://doi.org/10.1175/MWR-D-16-0480.1>

Roca, R., Fiolleau, T., & Bouniol, D. (2017). A simple model of the life cycle of mesoscale convective systems cloud shield in the tropics. *Journal of Climate*, 30(11), 4283–4298. <https://doi.org/10.1175/JCLI-D-16-0556.1>

Salathé, E. P., & Hartmann, D. L. (1997). A trajectory analysis of tropical upper-tropospheric moisture and convection. *Journal of Climate*, 10(10), 2533–2547. [https://doi.org/10.1175/1520-0442\(1997\)010\(2533:ATAOTU\)2.0.CO;2](https://doi.org/10.1175/1520-0442(1997)010(2533:ATAOTU)2.0.CO;2)

Satoh, M., Iga, S. I., Tomita, H., Tsushima, Y., & Noda, A. T. (2011). Response of upper clouds in global warming experiments obtained using a global nonhydrostatic model with explicit cloud processes. *Journal of Climate*, 25, 2178–2191. <https://doi.org/10.1175/JCLI-D-11-00152.1>

Seeley, J. T., & Romps, D. M. (2015). Why does tropical convective available potential energy (CAPE) increase with warming? *Geophysical Research Letters*, 42(23), 10429–10437. <https://doi.org/10.1002/2015GL066199>

Senf, F., Klocke, D., & Brueck, M. (2018). Size-resolved evaluation of simulated deep tropical convection. *Monthly Weather Review*, 146(7), 2161–2182. <https://doi.org/10.1175/MWR-D-17-0378.1>

Sherwood, S. C., Webb, M. J., Annan, J. D., Armour, K. C., Forster, P. M., Hargreaves, J. C., et al. (2020). An assessment of earth's climate sensitivity using multiple lines of evidence. *Reviews of Geophysics*, 58(4), 1–92. <https://doi.org/10.1029/2019rg000678>

Singh, M. S., Kuang, Z., Maloney, E. D., Hannah, W. M., & Woldring, B. O. (2017). Increasing potential for intense tropical and subtropical thunderstorms under global warming. *Proceedings of the National Academy of Sciences*, 114(44), 11657–11662. <https://doi.org/10.1073/pnas.1707603114>

Soden, B. J. (1998). Tracking upper tropospheric water vapor radiances: A satellite perspective. *Journal of Geophysical Research*, 103(D14), 17069–17081. <https://doi.org/10.1029/98JD01151>

Soden, B. J., Broccoli, A. J., & Hemler, R. S. (2004). On the use of cloud forcing to estimate cloud feedback. *Journal of Climate*, 17(19), 3661–3665. [https://doi.org/10.1175/1520-0442\(2004\)017<3661:OTUOCF>2.0.CO;2](https://doi.org/10.1175/1520-0442(2004)017<3661:OTUOCF>2.0.CO;2)

Soden, B. J., Held, I. M., Colman, R. C., Shell, K. M., Kiehl, J. T., & Shields, C. A. (2008). Quantifying climate feedbacks using radiative kernels. *Journal of Climate*, 21(14), 3504–3520. <https://doi.org/10.1175/2007JCLI2110.1>

Sokol, A. B., & Hartmann, D. L. (2020). Tropical anvil clouds: Radiative driving toward a preferred state. *Journal of Geophysical Research: Atmospheres*, 125(21), e2020JD033107. <https://doi.org/10.1029/2020JD033107>

Sprenger, M., & Wernli, H. (2015). The LAGRANTO Lagrangian analysis tool: Version 2.0. *Geoscience Model Device*, 8, 2569–2586. <https://doi.org/10.5194/gmd-8-2569-2015>

Strandgren, J. (2018). *The life cycle of anvil cirrus clouds from a combination of passive and active satellite remote sensing* (pp. 1–148). Munich, Germany, Ludwig Maximilian University. <https://doi.org/10.5282/edoc.22789>

Sun, J., Zhang, K., Wan, H., Ma, P. L., Tang, Q., & Zhang, S. (2019). Impact of nudging strategy on the climate representativeness and hind cast skill of constrained EAMv1 simulations. *Journal of Advances in Modeling Earth Systems*, 11(12), 3911–3933. <https://doi.org/10.1029/2019MS001831>

Tompkins, A. M., & Craig, G. C. (1999). Sensitivity of tropical convection to sea surface temperature in the absence of large-scale flow. *Journal of Climate*, 12(2), 462–476. [https://doi.org/10.1175/1520-0442\(1999\)012\(0462:SOTCTS\)2.0.CO;2](https://doi.org/10.1175/1520-0442(1999)012(0462:SOTCTS)2.0.CO;2)

Tsushima, Y., Iga, S. I., Tomita, H., Satoh, M., Noda, A. T., & Webb, M. J. (2015). High cloud increase in a perturbed SST experiment with a global nonhydrostatic model including explicit convective processes. *Journal of Advances in Modeling Earth Systems*, 6(3), 571–585. <https://doi.org/10.1002/2013MS000301>

van Diedenhoven, B., Ackerman, A. S., Fridlind, A. M., Cairns, B., & Riedi, J. (2020). Global statistics of ice microphysical and optical properties at tops of optically thick ice clouds. *Journal of Geophysical Research: Atmospheres*, 125(6), 1–21. <https://doi.org/10.1029/2019JD031811>

Van Diedenhoven, B., Fridlind, A. M., Cairns, B., Ackerman, A. S., & Yorks, J. E. (2016). Vertical variation of ice particle size in convective cloud tops. *Geophysical Research Letters*, 43(9), 4586–4593. <https://doi.org/10.1002/2016GL068548>

Wall, C. J., & Hartmann, D. L. (2018). Balanced cloud radiative effects across a range of dynamical conditions over the tropical West Pacific. *Geophysical Research Letters*, 5, 490–498. <https://doi.org/10.1029/2018GL080046>

Wall, C. J., Hartmann, D. L., Thieman, M. M., Smith, W. L., & Minnis, P. (2018). The life cycle of anvil clouds and the top-of-atmosphere radiation balance over the tropical West Pacific. *Journal of Climate*, 31(24), 10059–10080. <https://doi.org/10.1175/JCLI-D-18-0154.1>

Wang, M., & Zhang, G. J. (2018). Improving the simulation of tropical convective cloud-top heights in CAM5 with CloudSat observations. *Journal of Climate*, 31(13), 5189–5204. <https://doi.org/10.1175/JCLI-D-18-0027.1>

Webb, M., Senior, C. B., Bony, S., & Morcrette, J. J. (2001). Combining ERBE and ISCCP data to assess clouds in the Hadley Center, ECMWF and LMD atmospheric climate models. *Climate Dynamics*, 17(12), 905–922. <https://doi.org/10.1007/s003820100157>

Wernli, H., & Davies, H. C. (1997). A Lagrangian-based analysis of extratropical cyclones. 1. The method and some applications. *Quarterly Journal of the Royal Meteorological Society*, 123(538), 467–489. <https://doi.org/10.1256/smsqj.53810>

Wielicki, B. A., Barkstrom, B. R., Harrison, E. F., Lee, R. B., Smith, G. L., & Cooper, J. E. (1996). Clouds and the earth's radiant energy system (CERES): An earth observing system experiment. *Bulletin of the American Meteorological Society*, 77(5), 853–868. [https://doi.org/10.1175/1520-0477\(1996\)077\(0853:CATERE\)2.0.CO;2](https://doi.org/10.1175/1520-0477(1996)077(0853:CATERE)2.0.CO;2)

Wing, A. A., Stauffer, C. L., Becker, T., Reed, K. A., Ahn, M. S., Arnold, N. P., et al. (2020). Clouds and convective self-aggregation in a multimodel ensemble of radiative-convective equilibrium simulations. *Journal of Advances in Modeling Earth Systems*, 12(9), e2020MS002138. <https://doi.org/10.1029/2020MS002138>

Xie, S., Lin, W., Rasch, P. J., Ma, P.-L., Neale, R., Larson, V. E., et al. (2018). Understanding cloud and convective characteristics in Version 1 of the E3SM atmosphere model. *Journal of Advances in Modeling Earth Systems*, 10, 1–27. <https://doi.org/10.1029/2018MS001350>

Yoshimori, M., Lambert, F. H., Webb, M. J., & Andrews, T. (2020). Fixed anvil temperature feedback: Positive, zero, or negative? *Journal of Climate*, 33(7), 2719–2739. <https://doi.org/10.1175/jcli-d-19-0108.1>

Zelinka, M. D., & Hartmann, D. L. (2010). Why is longwave cloud feedback positive? *Journal of Geophysical Research*, 115(16), 1–16. <https://doi.org/10.1029/2010JD013817>

Zelinka, M. D., Klein, S. A., & Hartmann, D. L. (2012a). Computing and partitioning cloud feedbacks using cloud property histograms. Part I: Cloud radiative kernels. *Journal of Climate*, 25(11), 3715–3735. <https://doi.org/10.1175/JCLI-D-11-00248.1>

Zelinka, M. D., Klein, S. A., & Hartmann, D. L. (2012b). Computing and partitioning cloud feedbacks using cloud property histograms. Part II: Attribution to changes in cloud amount, altitude, and optical depth. *Journal of Climate*, 25, 3736–3754. <https://doi.org/10.1175/JCLI-D-11-00249.1>

Zelinka, M. D., Klein, S. A., Taylor, K. E., Andrews, T., Webb, M. J., Gregory, J. M., et al. (2013). Contributions of different cloud types to feedbacks and rapid adjustments in CMIP5. *Journal of Climate*, 26(14), 5007–5027. <https://doi.org/10.1175/JCLI-D-12-00555.1>

Zelinka, M. D., Zhou, C., & Klein, S. A. (2016). Insights from a refined decomposition of cloud feedbacks. *Geophysical Research Letters*, 43(17), 9259–9269. <https://doi.org/10.1002/2016GL069917>

Zhang, G. J., & McFarlane, N. A. (1995). Sensitivity of climate simulations to the parameterization of cumulus convection in the Canadian climate centre general circulation model. *Atmosphere-Ocean*, 33(3), 407–446. <https://doi.org/10.1080/07055900.1995.9649539>

Zhang, Y., Xie, S., Lin, W., Klein, S. A., Zelinka, M., Ma, P. L., et al. (2019). Evaluation of clouds in version 1 of the E3SM atmosphere model with satellite simulators. *Journal of Advances in Modeling Earth Systems*, 11, 1–16. <https://doi.org/10.1029/2018MS001562>

Zhao, M. (2014). An investigation of the connections among convection, clouds, and climate sensitivity in a global climate model. *Journal of Climate*, 27(5), 1845–1862. <https://doi.org/10.1175/JCLI-D-13-00145.1>

Zhao, M., Golaz, J. C., Held, I. M., Ramaswamy, V., Lin, S. J., Ming, Y., et al. (2016). Uncertainty in model climate sensitivity traced to representations of cumulus precipitation microphysics. *Journal of Climate*, 29(2), 543–560. <https://doi.org/10.1175/JCLI-D-15-0191.1>

Zhao, X., Lin, Y., Peng, Y., Wang, B., Morrison, H., & Gettelman, A. (2017). A single ice approach using varying ice particle properties in global climate model microphysics. *Journal of Advances in Modeling Earth Systems*, 9(5), 2138–2157. <https://doi.org/10.1002/2017MS000952>

Zhou, C., Dessler, A., Zelinka, M., Yang, P., & Wang, T. (2014). Cirrus feedback on interannual climate fluctuations. *Geophysical Research Letters*, 41(24), 9166–9173. <https://doi.org/10.1002/2014GL062095>

Zhu, J., & Poulsen, C. J. (2019). Quantifying the cloud particle-size feedback in an earth system model. *Geophysical Research Letters*, 46(19), 10910–10917. <https://doi.org/10.1029/2019GL083829>